Petroleum Science 23 (2026) 656–679

Contents lists available at ScienceDirect

Petroleum Science

journal homepage: www.keaipublishing.com/en/journals/petroleum-science

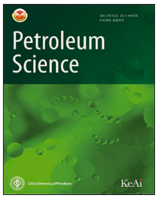

Original Paper

Permeability estimation using rock physics modeling and variational Bayes inversion

Mohammadfarid Ghasemi [a,*], Abdorrazagh Javid [b]

[a] Faculty of Earth Science, Shahid Beheshti University, 1983969411, Tehran, Iran
[b] Department of Earth and Atmospheric Sciences, University of Houston, Houston, 77204, Texas, USA

ARTICLE INFO

Article history:
Received 12 May 2025
Received in revised form
10 August 2025
Accepted 14 October 2025
Available online 18 October 2025

Edited by Meng-Jiao Zhou

Keywords:
Variational Bayes
Permeability
Well log data
Rock physics modelling
Carbonates

ABSTRACT

Permeability estimation is pivotal in reservoir characterization; however, prevailing methods lack a standardized approach. Traditionally reliant on core samples, permeability assessment encounters limitations across diverse thicknesses and wells. An innovative core-independent two-step rock physics template (RPT) can be designed to estimate elastic and conductive properties. The suggested RPT employs the T-matrix method to leverage well-log data encompassing porosity, fluid saturation, and various textural parameters. The estimation process for textural parameters involves addressing uncertainties through the fixed form variational inference (FFVB) with the trust region reflective optimization algorithm. These uncertainties span estimated textural parameters, seismic wave propagation velocity, electrical resistivity, and hydraulic permeability. Micro and macro voids, micro-spherical pores porosity, and their semi-axis are modeled using Beta distributions for both prior and variational families. The noise in the model assumes an inverse gamma distribution for sonic travel time and true formation resistivity. Validation of the proposed method is achieved by comparing the FFVB results with Metropolis Hasting's sampling method in three depths and also through geological observations and experimental analyses on available core samples. The inverse problem, involving the determination of textural parameters through sonic travel time and resistivity, is solved. Subsequently, the forward problem is addressed to estimate permeability. The robustness of the inverse problem is underscored by minimal discrepancies between measured sonic travel times, true formation resistivity values, and the results of the forward problem. The method demonstrates its effectiveness in permeability estimation, even in regions lacking core data, thereby emphasizing its reliability and applicability in diverse geological settings.

1. Introduction

The delineation of fractures within reservoirs assumes profound significance in optimizing hydrocarbon production, given their substantial impact on reservoir porosity and permeability. Consequently, the identification and characterization of naturally fractured areas in reservoirs pose a significant challenge for seismic investigations. The methods for estimating permeability as described in the existing literature can be categorized into two main types: (1) empirical and semi-empirical correlations and (2) predictive models based on effective medium theories. Empirical correlations can be developed from petrophysical properties derived from core data, well log data, or a combination of both. The relationships between these characteristics can be determined using multivariate regression analysis, numerical modeling, or advanced statistical learning techniques such as artificial neural networks and fuzzy logic regression. Semi-empirical correlations are those that have a mathematical basis but include some parameters that need to be determined experimentally. Below, we elaborate on the aforementioned methods.

The Kozeny-Carman relationship, founded on a tube-like model (Carcione and Avseth, 2015), offers a method to calculate permeability utilizing porosity and the Kozeny constant. Empirical relationships derived from the Kozeny-Carman theory connect permeability to other well logs or well-log-derived parameters

---

* Corresponding author.
E-mail address: mo_ghasemi@sbu.ac.ir (M. Ghasemi).
Peer review under the responsibility of China University of Petroleum (Beijing).

https://doi.org/10.1016/j.petsci.2025.10.011

like resistivity and irreducible water saturation (Bateman, 1985). However, these correlations are typically applied only to the region above the transition zone or the transition zone itself. In the absence of core data, Timur (1968) proposed a correlation involving irreducible water saturation, porosity, and permeability. Ahmed et al. (1991) extended Timur's model by incorporating the impact of minerals, introducing a dual water model for estimating permeability. However, the reliability of the results diminishes in complex, heterogeneous, or fractured reservoirs due to the relation of irreducible water saturation to shale volume and crystal size. Morris and Biggs (1967) devised an empirical correlation to predict permeability using porosity and resistivity-based saturation. Dorfman et al. (1990) applied the generalized Kozeny model to estimate permeability in heterogeneous carbonate formations using well logs. However, the use of a gas adsorption method to determine specific surface area and tortuosity presents challenges, with the approach proving inaccurate for formations with extremely low or high permeability. Saner et al. (1997) proposed an experimental relationship between permeability, water saturation, and rock resistivity. Despite its potential application for interpreting these parameters in the absence of information on the other two, the correlation may not consistently meet expectations due to pore geometry heterogeneity, common in reservoir rocks with similar porosity but different permeability. Granberry and Keelan (1977) elucidated relationships among permeability, water saturation, and porosity, yet the calculation of water saturation introduces uncertainty into permeability estimations (Ahmadi et al., 2013). Yao and Holditch (1993) introduced a permeability correlation model linking core permeability to open-hole log data, eliminating the need for specific values of irreducible water saturation or grain diameter.

Log–log-linear relationship between permeability and log data and particularly resistivity, is commonly employed as another class of regression analysis and empirical correlations (Archie, 1942; Wong et al., 1984; Purvance and Andricevic, 2000). This method, while efficient, introduces potential non-uniqueness and ambiguity in the relationship between permeability and resistivity due to factors such as water saturation and clay content, as well as potential scale and resolution disparities between permeability and resistivity measurements (Ezzedine et al., 1999). Despite utilizing multiple parameter regression and depth adjustments of core and log data, the use of semi-empirical equations limits the precision of permeability estimation. Johnson (1994) presented a method for accurately estimating permeability using well logs and available core data to identify distinct hydraulic zones based on pore structures. Wang et al. (2015) used an innovative approach and introduced a method to assess permeability using a mud-filtrate invasion model based on resistivity logs with varying investigation radii. Semmelbeck et al. (1995) introduced PermLog, a multidisciplinary method designed to forecast new generation induction logs without multiple repetitive logging runs. This model integrates a reservoir fluid flow simulator with the convection of dissolved species within a single phase, such as water or salt, predicting mud cake thickness and permeability under both static and dynamic filtration conditions. However, while the model accurately predicts certain aspects, it provides only an approximate value for permeability (Semmelbeck and Diyashev, 1996). Lin and Salisch (1994) employed the interconnection between porosity, permeability, and lithofacies, establishing an empirical correlation through regression to discern lithofacies. Another established method involves correlating permeability with Stoneley wave velocity by acoustic logging tools (Ahmed et al., 1991). Tang and Cheng (1996) introduced an algorithm to estimate formation permeability from Stoneley wave logs using a simplified Biot-Rosenbaum model.

Recent studies have explored direct and indirect relationships between seismic properties and permeability. Chork et al. (1994) introduced a straightforward approach for determining permeability using segmented sonic log data. Fundamental research by Klimentos (1991) established that P-wave velocity in sandstones is primarily governed by porosity and clay content, with permeability exerting negligible direct influence. This revealed that velocity-permeability relationships are inherently indirect, mediated through shared dependencies on pore geometry. Building on this understanding of textural controls, Prasad (2003) demonstrated that grouping rocks into hydraulic units based on porosity-permeability relationships significantly improves velocity-permeability correlations within each unit ($R^2 = 0.65 - 0.87$). This unit-based approach effectively bypasses lithological heterogeneity, enabling practical permeability prediction from velocity logs in stratified formations.

Beyond these direct correlations, Pride et al. (2003) identified a more fundamental physical link: they theorized that permeability information is encoded in seismic amplitudes through mesoscopic fluid-flow-induced attenuation. While theoretically promising, they noted that computational barriers prevent direct inversion of permeability from full-waveform data. This theoretical foundation was operationally advanced by Goloshubin et al. (2008), who developed a frequency-dependent attribute tied to fluid mobility (K/μ) by integrating Biot-scale flow with scattering effects - essentially translating Pride's attenuation mechanism into a measurable seismic property.

For reservoirs exhibiting complex pore systems, Wang et al. (2009) revealed that velocity deviations from matrix trends correlate strongly with permeability in fractured/vuggy carbonates, highlighting how pore geometry modifies the base relationships established by Klimentos. Similarly, Gomez et al. (2010) discovered permeability-dependent anomalies in the Vp-resistivity relationship of clean sandstones, showing that textural variations beyond porosity manifest in coupled geophysical responses. These studies collectively demonstrate how deviations from ideal velocity-porosity models serve as permeability indicators in heterogeneous media.

Finally, focusing specifically on fracture networks, Khromova et al. (2011) validated these principles through comparative analysis of seismic methods. Their finding that duplex wave migration (DWM) outperforms amplitude- and anisotropy-based techniques for fracture permeability prediction (achieving 25 m accuracy) confirms that specialized approaches are needed to resolve the complex velocity perturbations caused by fracture networks—effectively operationalizing the deviation concepts identified by Wang et al. (2009) and Gomez et al. (2010).

In addition to using simple multivariate regressions to establish empirical and semi-empirical relationships between well log data, core petrophysical data, and permeability, various other methods for estimating permeability include slug tests (Al-Mudhafar and Mohamed, 2015; Rafik and Kamel, 2017), drill stem tests (Bouwer and Rice, 1976; Bourdet et al., 1989; Al-Raoush and Willson, 2005; Kabir et al., 2011), neural networks (Mohaghegh et al., 1997; Lee et al., 2002), fuzzy logic (Nashawi and Malallah, 2009), and support vector regression (Al-Anazi and Gates, 2010). Artificial Neural Networks (ANN) have gained popularity in the petroleum industry due to their ability to generalize and perform nonlinear approximation (Mohaghegh et al., 1995; Huang and Williamson, 1996; Al Moqbel and Wang, 2011). Rogers et al. (1995) applied a backpropagation artificial neural network (BP-NN) to establish a permeability regression model using porosity logs as input.

The use of effective medium theories to estimate permeability in log and seismic scales is another approach, though these theories have inherent limitations. Some successful approaches may be applicable to low concentrations of inclusions, while others are suitable for high concentrations but overlook the inner structure of the porous medium (Jiang and Chesnokov, 2012; Jiang, 2013). Due to different assumptions, predictions of various effective medium theories may differ (Ali, 2011). Understanding rock physics and scaling issues is crucial to leverage connections between effective permeability and geophysical measurements, establishing a fundamental link between geophysical measurements and reservoir properties for effective correlation. However, rock physics models for carbonate reservoirs are less developed compared to those for sandstone reservoirs due to the complex characteristics of carbonate reservoirs, including porosity, pore shapes, and fractures (Zhao et al., 2013; Wang et al., 2017). Recent research suggests progress in developing carbonate rock physics models, but they remain insufficient (Ghon et al., 2018; Li and Zhang, 2018). Rocks often exhibit a significant presence of inclusions and diverse internal structures, similar to fractured carbonate reservoirs. In such cases, employing an effective medium theory capable of accounting for both high porosity and porous connectivity becomes necessary, allowing the calculation of effective properties for the closest possible agreement with experimental observations. It is essential to validate this theory using realistic data for accurate results.

This paper utilizes T-matrix (Jakobsen et al., 2003a,b; Jakobsen, 2006; Ali, 2011; Ali and Jakobsen, 2014), to evaluate the effective elastic and conductive (electrical and hydraulic) properties of the studied carbonate formation. For inversion we use the fixed form variational Bayes approach suggested and comprehensively described by Nawaz et al. (2020) and Zhang et al. (2021).

The paper is structured as follows: Utilizing well log data, we first assess petrophysical attributes. A two-scale dual porosity dual permeability rock physics template (RPT) is subsequently constructed to describe the relation between seismic wave velocity, electrical and hydraulic conductivities and hypothetical textural characteristics considered as model parameters. Fixed form variational Bayes method (Tran et al., 2021; Nawaz et al., 2020; Zhang et al., 2021) is then employed to address the inverse problem. The fixed form variational Bayes (FFVB) method, combined with the trust region reflective algorithm (Byrd et al., 1987), is used to resolve the inverse problem, providing estimates of constructed RPT model parameters in terms of posterior probability density rather than singular values. Analytical solutions for the Hessian of the variational function are derived, facilitating use of trust region reflective optimization algorithm. Metropolis Hastings sampling algorithm is then employed for 3 depths with different microfacies to validate the FFVB results. Finally, the FFVB inversion results are compared with the sedimentary and microfacies evidence, as well as the permeability values obtained from experimental results, to validate the employed RPT and assess the accuracy and robustness of the inversion. A detailed sedimentological and microfacies analysis is also provided in a separate supplementary information file.

All results were obtained using a MATLAB-based code package. The codes related to the variational Bayes and Metropolis Hasting's inversion are uploaded in https://github.com/MFarid110/Variational-Bayes-Inversion-MATLAB.git.

2. Methodology

2.1. The physical and mathematical description of the rock physics model

Rocks, particularly reservoir rocks, are natural composites with distinct internal structures. The requirements for a method to determine the macroscopic physical properties of such composites and its applicability can be formulated as follows (Bayuk, 2013):

- The components exhibit contrasting properties.
- The number and concentration of components are arbitrary.
- The rock's elastic and conductivity properties can be anisotropic without restriction on symmetry system.
- The method should account for differences in component shapes, orientations within the volume of the medium, and the degree of connectivity between components.

The challenge of determining the effective physical properties of composites boils down to describing the interaction among multiple bodies, a problem whose exact solution is generally impossible (Bethe, 1931; Kohn and Sham, 1965). Therefore, there exist numerous approximate methods for determining these properties, all based on different assumptions about the distribution of physical fields within composites. The accuracy of these approximate solutions depends on how closely these assumptions match reality.

As noted earlier, rock is a natural microscopically heterogeneous but macroscopically homogeneous composite material. If within such a micro-heterogeneous medium, a volume can be identified whose properties coincide with those of the entire medium on the scale being considered, this volume is termed representative volume element (RVE). The largest linear dimension of the RVE must be much larger than the size of the heterogeneity and much smaller than the wavelength in the case of elastic properties. The definition of the effective tensor of elastic and conductive properties $\mathbf{X}^*$ can be given in a generalized form (Shermergor, 1977; Willis, 1977):

$$\langle \mathbf{A}(\vec{\boldsymbol{r}}) \rangle = \mathbf{X}^* : \langle \mathbf{B}(\vec{\boldsymbol{r}}) \rangle, \tag{1}$$

In the context provided, $\mathbf{A}(\vec{\boldsymbol{r}})$ and $\mathbf{B}(\vec{\boldsymbol{r}})$ represent physical fields within an arbitrary vector. $\vec{\boldsymbol{r}}$ of the considered micro-heterogeneous medium, where the local relation holds as follows:

$$\mathbf{A}(\vec{\boldsymbol{r}}) = \mathbf{X}(\vec{\boldsymbol{r}}) : \mathbf{B}(\vec{\boldsymbol{r}}), \tag{2}$$

Here, the angular brackets denote the spatial and volumetric averaging over a representative volume (see (Ghasemi and Bayuk, 2020)). For elastic properties, $\mathbf{A}(\vec{\boldsymbol{r}})$ and $\mathbf{B}(\vec{\boldsymbol{r}})$ correspond to stress and strain tensors, respectively, while $\mathbf{X}(\vec{\boldsymbol{r}})$ represents the elasticity tensor. In this case, Eq. (1) and its local variant Eq. (2) adhere to Hooke's law. For thermal and electrical properties, these correspond to Fourier's and Ohm's laws, respectively. Specifically: Thermal properties involve heat flux density vectors $\mathbf{A}(\vec{\boldsymbol{r}})$, temperature gradient vectors $\mathbf{B}(\vec{\boldsymbol{r}})$ and the thermal conductivity tensor $\mathbf{X}(\vec{\boldsymbol{r}})$. Electrical properties involve current density vectors $\mathbf{A}(\vec{\boldsymbol{r}})$, electric field intensity vectors $\mathbf{B}(\vec{\boldsymbol{r}})$ and the electrical conductivity tensor $\mathbf{X}(\vec{\boldsymbol{r}})$. Hydraulic permeability properties involve fluid flow density vectors $\mathbf{A}(\vec{\boldsymbol{r}})$, pressure gradient vectors $\mathbf{B}(\vec{\boldsymbol{r}})$ and the hydraulic permeability tensor divided by the dynamic viscosity of the fluid $\mathbf{X}(\vec{\boldsymbol{r}})$. These relationships describe the effective behavior of the composite medium, incorporating the spatial and volumetric averaging necessary to capture its macroscopic properties from its heterogeneous microstructure. There are numerous approach to estimate the effective physical properties of a microscopically heterogeneous material like Mori-Tanaka's method (Mori and Tanaka, 1973), Kuster and Toksöz model (Kuster and Toksöz, 1974), Connell's approach (Watt et al., 1976), Hudson's crack model (Hudson, 1980), and differential effective medium theory (Norris, 1985). Most of these methods, with exception for Hudson's crack model, are restricted to the isotropic case and cannot account for anisotropy, which is crucial for accurately modelling materials with directional properties. Additionally, these methods exhibit instability when dealing with high porosity or high crack densities. This instability manifests as an underestimation of crack density and effective conductivity values, when solving geophysical inverse problems, respectively. To avoid these problems we choose T-matrix approach to estimate elastic moduli, electrical and hydraulic conductivity of the studied medium (Jakobsen et al., 2003a,b; Jakobsen, 2007; Shahraini et al., 2010; Sævik et al. 2012, 2013; Sævik et al., 2013a,b).

The effective stiffness tensor $\mathbf{C}^*$ in T-matrix approach can be formulated as follows (Jakobsen et al., 2003a,b):

$$\mathbf{C}^* = \mathbf{C}^{(0)} + \mathbf{t}_1 : \left(\mathbf{I}^{(4)} + \mathbf{G}^{(\mathrm{r})} : \mathbf{t}_1\right)^{-1}, \tag{3}$$

$$\mathbf{t}_1 = \langle \mathbf{t}^{(\mathrm{r})} \rangle, \tag{4}$$

$$\mathbf{t}^{(\mathrm{r})} = \mathbf{C}' : \left[\mathbf{I}^{(4)} - \mathbf{G}^{(\mathrm{r})} : \mathbf{C}'\right]^{-1}, \tag{5}$$

where $\mathbf{C}^*$ is the effective stiffness of the inhomogeneous original body. Again $\langle . \rangle$ means the average over spatial orientation and volumetric concentration. A double dot product refers to the contraction of two fourth rank tensors based on the last two values of the first tensor and the first two values of the second tensor. $\mathbf{C}^{(\mathrm{r})}$ is the stiffness tensor for r'th component. $\mathbf{G}$ is the second derivative of Green's function. $\mathbf{C}'$ is the stiffness difference between the r'th component and comparison body, $\mathbf{C}' = \mathbf{C}^{(\mathrm{r})} - \mathbf{C}^{(0)}$. In elasticity case, the expression of tensor $\mathbf{G}$ in spherical coordinate system for ellipsoidal inclusions can be written as (Shermergor, 1977; Bayuk and Chesnokov, 1998):

$$G_{ijkl} = -\frac{1}{16\pi}\int_0^{2\pi} \times \int_0^{\pi} \left(n_{kj}\Lambda_{il}^{-1} + n_{ki}\Lambda_{jl}^{-1} + n_{lj}\Lambda_{ik}^{-1} + n_{li}\Lambda_{jk}^{-1}\right) \sin\theta \mathrm{d}\theta \mathrm{d}\varphi, \tag{6}$$

$$\Lambda_{ik} = C_{ijkl}^{\mathrm{c}} n_{jl,} \tag{7}$$

$$n_{ij} = n_i n_{j,} \tag{8}$$

$$n_1 = \sin\theta \cos\varphi / a_1, \tag{9}$$

$$n_2 = \sin\theta \sin\varphi / a_2, \tag{10}$$

$$n_3 = \cos\theta / a_3, \tag{11}$$

where a_1, a_2, a_3 are the semi-axes of arbitrary ellipsoid which is assumed to be the shape of the effective grain of inhomogeneity. For the general case, $a_1 \neq a_2 \neq a_3$; thus, it can be used to approximate most of the shapes of pore space constituents, including spherical, penny-shaped, needle-shaped, rectangular, etc. C_{ijkl}^{c} is the stiffness of the comparison body.

To analyze conductivity, we adhere to the methodologies delineated by Sævik et al. (2012, 2013) and Sævik et al. (2014), which draw heavily from the foundational work of Torquato (2002) and Barthélémy (2009). These studies evaluate various effective medium models designed to predict the effective conductivity (hydraulic, electrical, and electromagnetic) of porous media. The models under consideration include Maxwell's approximation (Torquato, 2002), symmetric and asymmetric self-consistent approximations (Fokker, 2001), differential effective medium approximation (Torquato, 2002), and the T-matrix method (Jakobsen, 2006). Notably, the T-matrix and the symmetric and asymmetric self-consistent methods demonstrated greater consistency with the laminated bounds used to validate these methods across different fracture densities. The T-matrix formulation to estimate the effective conductivity of a porous medium is as follows (Jakobsen, 2006; Sævik et al., 2014):

$$\boldsymbol{R}^* = \boldsymbol{R}^{(0)} + \boldsymbol{R}_1 \cdot \left(\boldsymbol{I}^{(2)} + \boldsymbol{G}^{(\mathrm{r})} \cdot \boldsymbol{R}_1\right)^{-1}, \tag{12}$$

$$\boldsymbol{R}_1 = \langle \boldsymbol{r}^{(\mathrm{r})} \rangle, \tag{13}$$

where, $\boldsymbol{R}^*$, $\boldsymbol{R}^{(0)}$ are effective conductivity and conductivity of the embedding matrix. Again, we emphasize that, conductivity, encompasses electrical, electromagnetic, and hydraulic conductivity. $\boldsymbol{I}^{(2)}$ is the second rank unity tensor (a 3 by 3 matrix, with diagonal elements equal to one and other elements equal to zero). $\langle . \rangle$ means the average over spatial orientation and volumetric concentration. $\boldsymbol{t}^{(\mathrm{r})}$ is the t-matrix of inclusions of type (r) and can be defined as:

$$\boldsymbol{r}^{(\mathrm{r})} = \left(\boldsymbol{R}^{(\mathrm{r})} - \boldsymbol{R}^{(0)}\right) \cdot \left[\boldsymbol{I}^{(2)} - \boldsymbol{G}^{(\mathrm{r})} \cdot \left(\boldsymbol{R}^{(\mathrm{r})} - \boldsymbol{R}^{(0)}\right)\right]^{-1}, \tag{14}$$

where, $\boldsymbol{R}^{(\mathrm{r})}$ and $\boldsymbol{G}^{(\mathrm{r})}$ are the inclusion conductivity and field concertation tensors, respectively. $\boldsymbol{G}^{(\mathrm{r})}$, referred to as $\boldsymbol{P}^{(0)}$ in Barthélémy's original paper can be estimated using a complex numerical method described in his work. The method presented by Bayuk and Chesnokov (1998) is similar to the field concentration tensor for the effective elastic tensor discussed in Eqs. (7)–(12), and can also be used to estimate $\boldsymbol{G}^{(\mathrm{r})}$ (Bayuk and Chesnokov, 1998):

$$G_{ij} = -\frac{1}{4\pi}\int_0^{2\pi}\int_0^{\pi} \left(n_{ij}\Lambda^{-1}\right) \sin\theta \mathrm{d}\theta \mathrm{d}\varphi, \tag{15}$$

$$\Lambda = R_{ij}^{(0)} n_{ij}, \tag{16}$$

where $\Lambda = R_{ij}^{c} n_{ij}$. n_1, n_2, n_3 are defined the same as equation. Einstein summation convention is used here that the repeating indices denote summing over 1, 2, 3. $R_{ij}^{(0)}$ is the transport tensor which is the effective electrical and hydraulic conductivity tensors of the comparison body.

2.2. Rock physics model construction

In fractured reservoir characterization, it is standard to conceptualize the reservoir as an ensemble of matrix blocks separated by fractures and vugs (van Golf-Racht, 1982; Bratton et al., 2006). These matrix blocks contain microvoids that supply fluids to the interconnected fracture-vug network, where primary production occurs. Accurate representation of such systems requires differentiation between: (1) the microvoid system within the matrix blocks, and (2) the larger-scale fractures and vugs occupying the inter-block spaces.

When applying effective medium theories to predict elastic moduli and seismic velocities, inclusion size cannot be explicitly incorporated. Following Bayuk's hierarchical approach (Bayuk et al., 2008), we therefore construct sequential models where systems with smaller-scale inclusions are modeled first, and subsequently embedded within systems containing larger-scale inclusions. This necessitates using aspect ratios (relative dimensions of ellipsoidal semi-axes) to characterize void systems without absolute size dependence.

Conversely, conductive property modeling (hydraulic/electrical) requires direct incorporation of inclusion dimensions. For these properties, we must utilize absolute semi-axis lengths rather than aspect ratios.

Our two-stage model implements this framework as follows:

1. The initial stage represents matrix blocks using ellipsoidal microvoids characterized by semi-axes ($\alpha_{\text{micro}}^{(1)\text{void}}, \alpha_{\text{micro}}^{(2)\text{void}}, \alpha_{\text{micro}}^{(3)\text{void}}$).
2. The subsequent stage embeds these blocks within a macrovoid system represented by ellipsoidal inclusions with semi-axes ($\alpha_{\text{macro}}^{(1)\text{void}}$, $\alpha_{\text{macro}}^{(2)\text{void}}$, $\alpha_{\text{macro}}^{(3)\text{void}}$), modeling interconnected fractures and vugs that separate matrix blocks.

This hierarchical approach preserves the standard conceptualization of fractured reservoirs while respecting the distinct theoretical requirements for elastic versus conductive property prediction.

In the first stage, micro voids with different semi-axes $a_1 \neq a_2 \neq a_3$ and micro spherical pores with equal semi-axes $a_1 = a_2 = a_3$, are incorporated into the effective electrical conductivity and effective stiffness tensor of a dual porosity dual permeability model. This model assumes that the pore space consists of micro voids and micro spherical pores. By integrating these inclusions into an isotropic embedding matrix with elastic, electrical conductivity, and hydraulic permeability tensors, and applying T-matrix homogenization methods, the embedding matrix for the next-scale model is obtained. In the second stage, macro voids are considered constituents of the embedding matrix obtained from the previous stage. The embedding matrix in the micro-scale model represents a medium composed of minerals. Fig. 1 provides a general representation of the proposed two-stage model with the known and unknown parameters at each stage. In the inverse problem, these microstructural parameters are unknown. The initial step in computing the effective elastic and conductive tensors involves determining several known parameters: water and hydrocarbon saturations, their bulk moduli, mineral types along with their volumetric concentrations and bulk moduli, density, electrical conductivity of formation water, and matrix conductivity. Water and hydrocarbon saturations, as well as mineral volumetric concentrations, are derived from well log data and the results are provided from industry well reports.

For the well, considered in this study, geological analysis indicates that the formation primarily comprises calcite and clay minerals, assumed to be isotropic and spherical (no preferred orientation). Despite ultrasonic measurements (Peselnick and Robie, 1962) and Brillouin spectroscopy (Chen et al., 2001) showing that calcite possesses an anisotropic stiffness tensor, it is a common practice to treat calcite minerals as isotropic, with bulk and shear moduli of 65 and 28 GPa, respectively, and a density of 2.71 g/cm^3 as indicated in chapter 4 of Mavko et al., 2020.

In the absence of XRD/XRF experimental data for the samples from the studied wellbore, we assumed that the clay minerals are predominantly illite and smectite, as suggested by Carcione and Avseth (2015). The ratio between these minerals can then be estimated using the sixth-order Arrhenius equation, as detailed by Carcione and Avseth (2015). Illite, an anisotropic mineral with a transversely isotropic system (Sams and Andrea, 2001; Bayuk et al., 2007; Sayers and den Boer, 2018) and a platy form, can induce anisotropy in the system due to its mineralogical structure and morphological characteristics. To simplify the model and avoid additional unknown parameters, we assumed the clay minerals to be penny shaped ($a_1 = a_2 > a_3$) , with fixed aspect ratio of ~1/30. This value can change from 1/50 to 1/10 according to Bayuk et al. (2007). The stiffness matrix of illite water composite in the present of smectite is $C_{11} = 23.7$, $C_{33} = 8.5$, $C_{44} = 0.8$, $C_{66} = 5.7$, $C_{13} = 3.1$ GPa, and a density of 2.17 g/cm^3 (Bayuk et al., 2007).

The bulk modulus and density of water are considered to be 2.25 GPa and 1.0 g/cm^3, respectively. More precise values, depending on pressure and temperature, can be obtained using the equations provided by Batzle and Wang (1992). As oil and gas properties are highly sensitive to pressure and temperature, their bulk moduli and densities at each depth are estimated using Eqs. (8)–(11b) for gases, and Eqs. (18)–(20b) for oils from Batzle and Wang (1992).

Matrix electrical and hydraulic conductivities were selected based on the discussions by Sævik et al. (2014) and Barthélémy (2009). The matrix is considered hydraulically and electrically resistive with $\boldsymbol{R}^{(\text{r})} \gg \boldsymbol{R}^{(0)}$. According to Barthélémy (2009), the hydraulic conductivity of inclusions is given by $\frac{b^2}{12}$, where b is the fracture aperture. Next, we should estimate the voids electrical conductivity takin into account their surface conductivity. According to the description provided in introduction section, in this study we aim to account for surface conductivity of voids in addition to the bulk conductivity which is due to the NaCl or

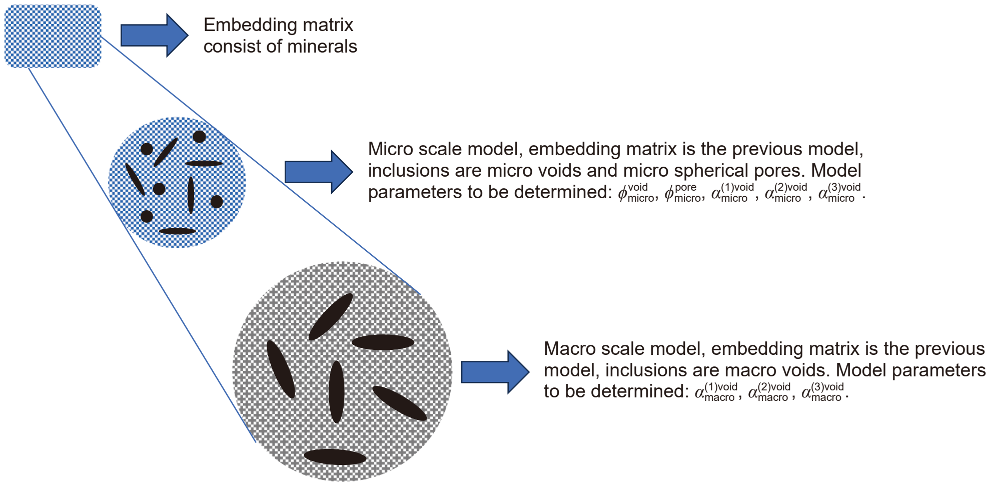

Fig. 1. General representation of the proposed two-stage rock physics modeling.

equivalent NaCl concertation of formation water saturating the voids. To do this we follow the procedure introduced by Revil and Glover (1997), Revil and Glover (1998), Revil et al. (1999) and Revil (2013). Since the equations related to estimate the surface electrical conductivity are more related to electrochemistry, we provide these equations in Appendix A.

Surface conductivity and ionic transport at mineral surfaces are significant phenomena applicable to all minerals, not just clay minerals. Several researchers, including Moulin and Roques (2003), Heberling et al. (2011), Li et al. (2016) and Al Mahrouqi et al. (2017) have conducted modeling and measurement studies of surface conductivity in carbonates. Integrating surface conductivity does not imply neglecting the bulk conductivity of the aqueous solution; rather, it involves accounting for both effects simultaneously. In this study, Eq. (A.3) demonstrates the coupling approach for surface and bulk conductivity, as proposed by Revil and Glover (1997). The dominance of surface or bulk electrical conductivity is influenced by factors such as pH and the ionic concentration of the aqueous solution. Analyzing the dominance range and presenting corresponding figures, as illustrated in Revil's work (Figs. 3–9), falls outside the scope of this manuscript. Readers interested in a more detailed discussion of the coupling mechanisms and the dominance of surface and bulk ionic conductivities are encouraged to consult the referenced articles for further insights.

Unknown parameters in the first step model include the semi-axis lengths of micro voids, along with their volumetric concentration (referred to as microporosity). For the second step, the first step results are considered the embedding matrix. Unknown parameters in the second step model include the semi-axes of macro voids with their volumetric concentration, termed macro porosity, which is equal to the total porosity minus the microporosity. A comprehensive sensitivity analysis of the employed rock physics methods to the microstructural parameters is available in Barthélémy (2009) and Sævik et al. (2014). In the next section we present the results of the extensive sensitivity analysis on the developed rock physics models. The inversion process is then conducted on the constructed rock physics models to estimate the mentioned unknown parameters using the measured wireline log data see Fig. 3.

2.3. Well log data interpretation

As previously discussed, despite the microstructural characteristics, the petrophysical attributes essential for the proposed rock physics template (RPT) are presumed to be known. These attributes encompass shale volume, both total and effective porosity, bulk density, fluid saturation, and mineral composition.

2.3.1. Shale volume estimation

According to Crain's handbook (Crain, 2021) several methodologies are employed to gauge shale volume from well log data, encompassing corrected and spectral gamma ray logs, SP log, resistivity log, neutron porosity-neutron density cross plot, and sonic density cross plot analyses. The most reliable technique entails deducing thorium content from spectral gamma logs. Nonetheless, the SP log may inaccurately represent shale volume in regions with heightened resistivity, with its precision diminishing in environments of fresh water or saline mud. The density neutron cross plot proves effective in discerning oil or water-bearing shaly sands but is ill-suited for dolomite, anhydrite, or gas-bearing regions. Similarly, the sonic density cross plot exhibits diminished accuracy in shallow shaly sands and is not recommended for gas-rich zones. Should spectral gamma ray logs be unavailable, shale volume estimation can be achieved using corrected gamma ray logs.

2.3.2. Total and effective porosity estimation

A comprehensive discussion is provided in Crain's handbook within the “Porosity Indicating Logs” section. The determination of total and effective porosity values utilizes a sophisticated complex lithology model for density neutron cross plot analysis. This method is favored over alternatives such as the shaly sand model or dual water model. The algorithm of the complex lithology model may also be applied to sonic density cross plot analysis, proving optimal in shaly sands devoid of gas. However, its resolution is compromised in carbonates, and the presence of gas may yield inflated results.

2.3.3. Water saturation

Nearly all saturation computation methods stem from Archie's seminal work (Archie, 1942), which delineates the relationship between formation resistivity and water saturation in clean sandstones. Various modifications have been proposed to incorporate the shale volume's effect on resistivity values, such as the Simandoux equation (Simandoux, 1963), Waxman-Smits's equation (Waxman and Smits, 1968), Indonesia equation (Poupon and Leveaux, 1971), and the dual water model, which should be utilized alongside the dual water porosity method and resembles the Simandoux equation. To the best of our knowledge, no definitive preference exists among these methods.

2.3.4. Oil and gas saturation, mineral content

The determination of oil and gas saturation and mineral content involves employing the material balance equation. This assumes a linear response log for neutron density and neutron porosity and utilizes the Raymer time-average equation (Raymer et al., 1980) for formation sonic travel time, solving these equations concurrently. For detailed algorithms and equations, one may refer to Crain's petrophysics handbook within the “Deterministic Analysis” section.

The estimation process for shale volume, total and effective porosity, fluid saturation, and mineral content constitutes an iterative hierarchical algorithm aimed at minimizing the discrepancy between well log data and their corresponding response equations. This is achieved by carefully selecting and refining the described petrophysical parameters throughout the iterative process. The above interpretation scheme is visualized in Fig. 3. We employed thorium content to estimate shale volume, complex lithology model to compute total and effective porosity, and the Indonesia model for water saturation assessment.

It is noteworthy that the presentation deliberately omits the inclusion of equations and detailed algorithms for well log interpretation to ensure conciseness. For an inquisitive reader seeking a thorough understanding of the methodology employed in interpreting well log data, reference to Crain's Petrophysics Handbook is recommended for an excellent explanation.

2.4. Variational Bayes inference

There is a growing need for Bayesian computation methods capable of managing large datasets and complex models with many unknown parameters. Traditional sampling methods like Markov Chain Monte Carlo (MCMC) and Sequential Monte Carlo (SMC) face scalability issues, particularly with contemporary applications such as deep neural networks and more traditional fields like graphical and mixture modeling. In response, variational Bayes (VB) provides an optimization-based solution for approximate Bayesian inference, proving to be a more computationally efficient alternative to these sampling techniques. VB is a part of the broader set of variational inference methods, which are also applicable in frequentist approaches for tasks like maximum likelihood estimation in the presence of missing data.

In Bayesian settings, VB focuses on approximating the posterior distributions (Tran et al., 2021):

$$p(\theta|y)=\frac{p(y,\theta)}{p(y)}=\frac{p(\theta)\ell(y|\theta)}{p(y)}\propto p(\theta)p(y|\theta), \tag{17}$$

where θ denotes the parameters, and y represents the data, Bayesian inference aims to capture all information about θ in its posterior distribution derived from the prior distribution $p(\theta)$ and the likelihood $\ell(y|\theta)$. The process involves computing the following integral (Tran et al., 2021):

$$p(y)=\int p(\theta)\ell(y|\theta)\mathrm{d}\theta \tag{18}$$

which determines the marginal likelihood or evidence. This integral is essential but challenging to calculate directly, especially without the normalizing constant $p(y)$, often ignored in analysis.

Traditional Bayesian analysis calculates expectations like the posterior mean from this distribution, but complexities arise from the intractable density $p(\theta|y)$. While MCMC methods address this by sampling, VB offers a quicker alternative by using a tractable distribution $q^*(\theta|\lambda)$ hereinafter refer to as q_λ^* from a family $\mathscr{Q}$, such as Gaussians, and minimizing the Kullback-Leibler (KL) divergence to optimize the following approximation with respect to λ (Tran et al., 2021):

$$q_\lambda^*=\arg\min\nolimits_{q\in\mathscr{Q}}\left\{\mathrm{KL}(q_\lambda\|p(\cdot|y))=\int q_\lambda(\theta)\log\frac{q_\lambda(\theta)}{p(\theta|y)}\mathrm{d}\theta\right\}. \tag{19}$$

where λ are the variational parameters that control the shape and location of $q_\lambda(\theta)$. The choice of this family should balance flexibility for approximating the true posterior with simplicity for tractable optimization. VB thus simplifies Bayesian inference by substituting the intractable posterior with a tractable approximation, enhancing computation and analysis. The minimization of KL divergence Eq. (19) effectively maximizes the lower bound (LB) on the log of the marginal likelihood $p(y)$ (Tran et al., 2021):

$$\begin{aligned}\mathrm{LB}(q_\lambda)&=\int q_\lambda(\theta)\log\frac{p(\theta)\ell(y|\theta)}{q_\lambda(\theta)}\mathrm{d}\theta=\mathbb{E}_{q_\lambda}\left(\log\frac{p(\theta)\ell(y|\theta)}{q_\lambda(\theta)}\right)\\&=\mathbb{E}_{q_\lambda}(h_\lambda(\theta)),\end{aligned} \tag{20}$$

where, $h_\lambda(\theta)=\log\frac{p(\theta)\ell(y|\theta)}{q_\lambda(\theta)}$ and $\mathbb{E}_{q_\lambda(\theta)}[f(\theta)]$ is a notation for the expected value of a function of $f(\theta)$ under the distribution q with parameter λ. It is defined as (Blei et al., 2017):

$$\mathbb{E}_{q_\lambda(\theta)}[f]=\int f(\theta)q_\lambda(\theta)\mathrm{d}\theta, \tag{21}$$

The $\mathrm{LB}(q_\lambda)$ can be interpreted as a lower bound on the log marginal likelihood of the data, $\log p(y)$, which is independent of λ. Therefore, maximizing the $\mathrm{LB}(q_\lambda)$ with respect to λ, Eq. (19) is equivalent to minimizing the KL divergence between $q_\lambda(\theta)$ and $p(\theta|y)$ (Eq. (20)). Variational Bayes algorithms (how to solve for Eq. (20)) fall into two categories: mean field VB (MFVB) and fixed form VB (FFVB), depending on the constraints applied to $\mathscr{Q}$. In MFVB we can we can obtain analytical expressions for integral in Eq. (20) (Tran et al., 2021). In the framework of FFVB, no constraints are imposed on $\mathscr{Q}$, rendering the derivation of an analytical expression for Eq. (20) potentially unfeasible. Consequently, it is advisable to approximate Eq. (20) by generating a substantial volume of random samples from the distribution $q(\theta)$ and subsequently assessing the expression $\mathbb{E}_{q_\lambda}\left(\log\frac{p(\theta)\ell(y|\theta)}{q_\lambda(\theta)}\right)$ through numerical methods.

For inversion of the constructed rock physics templates, we use the FFVB since the analytical expression for MFVB is intractable.

2.5. *Incorporating the rock physics model unknown parameters in variational Bayes inversion*

For our case we define the Model as follows:

2.5.1. *The prior distributions*

The model parameters which should be estimated are as follows (here we denoted the set of model parameters as θ):

Micro voids porosity, denoted as $\phi_{\mathrm{micro}}^{\mathrm{void}}$.

Micro spherical pores porosity, denoted as $\phi_{\mathrm{micro}}^{\mathrm{pore}}$.

Microvoids semi-axis, denoted as $\alpha_{\mathrm{micro}}^{(1)\mathrm{void}}$, $\alpha_{\mathrm{micro}}^{(2)\mathrm{void}}$, $\alpha_{\mathrm{micro}}^{(3)\mathrm{void}}$.

Macrovoids semi-axis, $\alpha_{\mathrm{macro}}^{(1)\mathrm{void}}$, $\alpha_{\mathrm{macro}}^{(2)\mathrm{void}}$, $\alpha_{\mathrm{macro}}^{(3)\mathrm{void}}$.

The sampling noises associated with compressional wave velocity and resistivity represent a distinctive aspect of Bayesian inversion, setting it apart from routine inversions. In routine inversions, such noises are typically not considered or incorporated into the analysis.

Establishing the prior distributions necessitates the incorporation of all available user information. One approach is to propose a diffuse (uninformative) distribution with a predetermined mean value but a substantial standard deviation (Spikes et al., 2007; Bosch et al., 2010).

The micro voids porosity values falling within the range of zero to some value less than one make the choice of the beta distribution appropriate. Similarly, when dealing with semiaxis values up to the millimeter scale, selecting the beta distribution is also justified, as it can effectively describe variables with limited ranges and continuous values within those boundaries. It's a common practice to select the inverse gamma distribution for describing sampling noise. The model parameters and their respective priors are listed in Table 3. We selected the priors so that the structural parameters are close to their respective mean values on a logarithmic scale, with sufficiently large standard deviations. This approach can be a good choice for unbiased and diffuse priors, as described by Berger and Bernardo (1991) and Robert (2007). The selection of priors is an arbitrary process, and readers can adjust the prior properties based on their knowledge or the specifics of their particular problem (Nawaz et al., 2020; Zhang et al., 2021).

2.5.2. *The variational family*

The probabilities under consideration as prior model parameters can also serve as a variational family for these parameters. However, in contrast to the case of priors where we assumed shape and scale parameters, the shape and scale parameters for these probabilities are currently unknown and require estimation through a robust and dependable optimization algorithm.

2.5.3. *The objective function*

In this stage, we defined the parameters of the rock physics model to be determined, the sampling noises for velocity and true formation resistivity measurements, their prior distribution, loss function, and variational family. The next step involves consolidating all the aforementioned details into a final equation, which will serve as the cornerstone for the optimization algorithm. For our case we can write:

$$\begin{aligned}
&\ell\left(\theta|\mathfrak{L}\left(y^{\text{est}},y^{\text{meas}}\right)\right)\\
&=\left\{-\frac{1}{2}\left(\frac{V^{(\text{est})}-V^{(\log)}}{\sigma^{(\text{velocity})}}\right)^{2}-\ln\sigma^{(\text{velocity})}-\frac{1}{2}\ln(2\pi)\right\}\\
&+\left\{-\frac{1}{2}\left(\frac{R^{(\text{est})}-R^{(\log)}}{\sigma^{(\text{resistivity})}}\right)^{2}-\ln\sigma^{(\text{resistivity})}-\frac{1}{2}\ln(2\pi)\right\},
\end{aligned} \tag{22}$$

where, $\ell(.)$ denotes the likelihood, $V^{(\text{est})}$, $R^{(\text{est})}$ are compressional/shear elastic waves velocities and true formation resistivities estimated through the proposed RPT model respectively. $V^{(\log)}$ and $R^{(\log)}$ are measured compressional/shear elastic waves velocities and true formation resistivities obtained from the available well log data. $\sigma^{(\text{velocity})}$ and $\sigma^{(\text{resistivity})}$ are the sampling noise variance for compressional/shear elastic waves velocities and true formation resistivity measurements.

$$\begin{aligned}
p(\theta)=&\left\{a^{(1)}\times\ln\left(b^{(1)}\right)-\ln\Gamma\left(a^{(1)}\right)-\left(a^{(1)}+1\right)\ln\left(\sigma^{(\text{velocity})}\right)\right.\\
&\left.-\frac{b^{(1)}}{\sigma^{(\text{velocity})}}\right\}+\left\{a^{(2)}\times\ln\left(b^{(2)}\right)-\ln\Gamma\left(a^{(2)}\right)\right.\\
&\left.-\left(a^{(2)}+1\right)\ln\left(\sigma^{(\text{resistivity})}\right)-\frac{b^{(2)}}{\sigma^{(\text{resistivity})}}\right\}\\
&+\sum_{i=2}^{10}\left(a^{(i)}-1\right)\ln\theta_i+\left(b^{(i)}-1\right)\ln(1-\theta_i)-\ln\beta\left(a^{(i)},b^{(i)}\right),
\end{aligned} \tag{23}$$

$$\begin{aligned}
q(\theta)=&\left\{a'^{(1)}\times\ln\left(b'^{(1)}\right)-\ln\Gamma\left(a'^{(1)}\right)-\left(a'^{(1)}+1\right)\ln\left(\sigma^{(\text{velocity})}\right)\right.\\
&\left.-\frac{b'^{(1)}}{\sigma^{(\text{velocity})}}\right\}+\left\{a'^{(2)}\times\ln\left(b'^{(2)}\right)-\ln\Gamma\left(a'^{(2)}\right)\right.\\
&\left.-\left(a'^{(2)}+1\right)\ln\left(\sigma^{(\text{resistivity})}\right)-\frac{b'^{(2)}}{\sigma^{(\text{resistivity})}}\right\}\\
&+\sum_{i=2}^{10}\left(a'^{(i)}-1\right)\ln\theta_i+\left(b'^{(i)}-1\right)\ln(1-\theta_i)-\ln\beta\left(a'^{(i)},b'^{(i)}\right),
\end{aligned} \tag{24}$$

where $p(\theta)$ and $q(\theta)$ are the prior distributions and variational family distributions respectively. $a^{(i)}$ and $b^{(i)}$ are the prior distribution shape and scale parameters (see Table 3), predefined, $a'^{(i)}$ and $b'^{(i)}$ are parameters of the variational family distribution (λ).

The rock physics model parameters, denoted as θ_i, have been previously delineated. We have presented the distribution for each individual parameter without any simplification to ensure that the reader can fully grasp the intricacies of the implementation process. To calculate the expected value $\mathbb{E}_{q_\lambda(\theta)}\left\{\log\frac{p(\theta)\ell(\theta|y)}{q_\lambda(\theta)}\right\}$ (Eq. (20)), it is essential to generate an adequate amount of data from the variational family distributions for each model parameter θ_i, corresponding to the suggested λ, in every optimization iteration. Following this, the value of $\log\frac{p(\theta)\ell(\theta|y)}{q_\lambda(\theta)}$ is computed, facilitating the straightforward acquisition of the average value.

2.6. *Trust-region-reflective algorithm for maximizing the lower bound (LB) on the log of the marginal likelihood $p(y)$*

The trust region reflective algorithm offers several advantages over stochastic gradient descent:

Divergence mitigation: Trust region reflective algorithm is less prone to divergence issues compared to stochastic gradient descent, providing a more stable optimization process.

- Global convergence: It tends to exhibit global convergence, meaning it is more likely to converge to the global minimum rather than getting stuck in local minima.
- Robustness to noisy data: Trust region reflective algorithm is robust in the presence of noisy or uncertain data, making it suitable for scenarios with imperfect information.
- Efficient optimization: It efficiently optimizes functions without the need for excessive tuning of hyperparameters, contributing to a more straightforward implementation.
- Adaptability to non-convex problems: It is well-suited for non-convex optimization problems, where the objective function may have multiple minima and maxima.

The TRRA algorithm has been integrated into various software packages, including Python, Matlab, and R. To use this algorithm in these packages, it is necessary to define the functions for gradient and hessian. The gradient in Eq. (16) of (Tran et al., 2021) as follows:

$$\nabla_\lambda\text{LB}(\lambda)=\mathbb{E}_{q_\lambda(\theta)}\{\nabla_\lambda[\ln q_\lambda(\theta)]\times h_\lambda(\theta)\}. \tag{25}$$

Here we derive the equation for Hessian as follows:

$$\begin{aligned}
\mathscr{H}_\lambda\text{LB}(\lambda)=&\int\nabla_\lambda[q_\lambda(\theta)](\nabla_\lambda[\ln q_\lambda(\theta)])^{\mathrm{T}}\times h_\lambda(\theta)+q_\lambda(\theta)\\
&\times\mathscr{H}_\lambda[\ln q_\lambda(\theta)]\times h_\lambda(\theta)-q_\lambda(\theta)\\
&\times\nabla_\lambda[\ln q_\lambda(\theta)](\nabla_\lambda[\ln q_\lambda(\theta)])^{\mathrm{T}}\mathrm{d}\theta\\
=&\int q_\lambda(\theta)\times\left\{\nabla_\lambda[\ln q_\lambda(\theta)](\nabla_\lambda[\ln q_\lambda(\theta)])^{\mathrm{T}}\right.\\
&\times h_\lambda(\theta)+\mathscr{H}_\lambda[\ln q_\lambda(\theta)]\times h_\lambda(\theta)\\
&\left.-\nabla_\lambda[\ln q_\lambda(\theta)](\nabla_\lambda[\ln q_\lambda(\theta)])^{\mathrm{T}}\right\}\mathrm{d}\theta\\
=&\mathbb{E}_{q_\lambda(\theta)}\left\{\left[\nabla_\lambda[\ln q_\lambda(\theta)](\nabla_\lambda[\ln q_\lambda(\theta)])^{\mathrm{T}}+\mathscr{H}_\lambda[\ln q_\lambda(\theta)]\right]\right.\\
&\left.\times h_\lambda(\theta)-\nabla_\lambda[\ln q_\lambda(\theta)](\nabla_\lambda[\ln q_\lambda(\theta)])^{\mathrm{T}}\right\}\\
=&\mathbb{E}_{q_\lambda(\theta)}\left\{\left[\nabla_\lambda[\ln q_\lambda(\theta)](\nabla_\lambda[\ln q_\lambda(\theta)])^{\mathrm{T}}+\mathscr{H}_\lambda[\ln q_\lambda(\theta)]\right]\right.\\
&\left.\times h_\lambda(\theta)-\nabla_\lambda[\ln q_\lambda(\theta)](\nabla_\lambda[\ln q_\lambda(\theta)])^{\mathrm{T}}\right\}\\
=&-\mathbb{E}_{q_\lambda(\theta)}\left(\nabla_\lambda[\ln q_\lambda(\theta)](\nabla_\lambda[\ln q_\lambda(\theta)])^{\mathrm{T}}\right).
\end{aligned} \tag{26}$$

The equation presented above was derived by utilizing an unverified equation within the scope of this article. The equation is as follows: $\mathbb{E}_{q_\lambda(\theta)}((\nabla_\lambda[\ln q_\lambda(\theta)])=0)$. We can also easily obtain that $\mathbb{E}_{q_\lambda(\theta)}(\mathscr{H}_\lambda[\ln q_\lambda(\theta)])=-\mathbb{E}_{q_\lambda(\theta)}\left(\nabla_\lambda[\ln q_\lambda(\theta)](\nabla_\lambda[\ln q_\lambda(\theta)])^{\mathrm{T}}\right)$. The demonstration of these equations is straightforward. Inserting Eqs.

(25) and (26) in Eq. (20) and attempting to solve the quadratic optimization problem often fails to converge due to the high variance associated with Eqs. (25) and (26). As outlined by Tran et al. (2021), three strategies can be employed to mitigate this variance: 1) employing the control variate method, 2) utilizing the natural gradient approach, and 3) implementing the reparameterization trick. As described by Tran et al. (2021), a Monte Carlo approximator of Eqs. (25) and (26) for i-th element of λ, the λ_i , can be written as:

$$\nabla_\lambda \mathrm{LB}(\lambda) = \frac{1}{S}\sum_{i=1}^{S}\left[\nabla_{\lambda_i}[\ln q_\lambda(\theta_s)]\right]\circ h_\lambda(\theta_s), \tag{27}$$

and

$$\mathscr{H}_\lambda \mathrm{LB}(\lambda) = \frac{1}{S}\sum_{i=1}^{S} -\nabla_\lambda[\ln q_\lambda(\theta_s)](\nabla_\lambda[\ln q_\lambda(\theta_s)])^{\mathrm{T}}, \tag{28}$$

where $\circ$ denotes the elementwise multiplication, and θ_s is “S” sample from variational distribution $q_\lambda(\theta)$ $(\theta_s \sim q_\lambda(\theta))$. As we mentioned before the variance of these estimators are too high to be used in the TRRA. In order to reduce the variance we employ the control variate approach (Tran et al., 2021). To do so we rewrite Eq. (25) as follows:

$$\nabla_{\lambda_i} \mathrm{LB}(\lambda) = \frac{1}{S}\sum_{i=1}^{S}\nabla_{\lambda_i}[\ln q_\lambda(\theta_s)]\circ h_\lambda(\theta_s) - c_i^{\nabla}\nabla_{\lambda_i}[\ln q_\lambda(\theta_s)], \tag{29}$$

which are still an unbiased estimator of Eq. (25), since $\mathbb{E}_{q_\lambda(\theta)}(\nabla_{\lambda_i} \ln q_\lambda(\theta)) = 0$, whose variance be greatly reduced by proper choice of c_i^{∇}. The value for c_i^{∇} is obtained by Tran et al. (2021) as follows:

$$c_i^{\nabla} = \frac{cov(\nabla_{\lambda_i}[\ln q_\lambda(\theta)] \times h_\lambda(\theta), \nabla_{\lambda_i}[\ln q_\lambda(\theta)])}{\mathbb{V}(\nabla_{\lambda_i}[\ln q_\lambda(\theta)])}, \tag{30}$$

The utilization of an optimization algorithm that incorporates the Hessian matrix of the objective function allows for a more efficient exploration of the λ-space geometry. By scaling the gradient vector with what is known as a natural gradient, we can enhance the convergence rate. This natural gradient guides the optimization process in the steepest direction, facilitating the optimization of the LB(λ) objective function on the manifold formed by the family of $q_\lambda(\theta)$ distributions. The natural gradient can be constructed by taking the regular gradient and multiplying it by the inverse of the Fisher information matrix. (Eq. (5.10) of Lehmann and George (1998)):

$$\nabla_\lambda^{\mathrm{nat}}[\ln q_\lambda(\theta)] = \mathbf{I}_F^{-1}(\lambda)\nabla_\lambda[\ln q_\lambda(\theta)], \tag{31}$$

where

$$\mathbf{I}_F(\lambda) = \mathbb{E}_{q_\lambda(\theta)}\left(-\nabla_\lambda[\ln q_\lambda(\theta)](\nabla_\lambda[\ln q_\lambda(\theta)])^{\mathrm{T}}\right). \tag{32}$$

To enhance the likelihood of achieving convergence while reducing computational time, the maximum a posteriori probability (MAP) estimate can be employed as an initial guess for the TRRA. However, it's important to note that in most scenarios, treating this value as the ultimate solution can be misleading. In fact, the MAP estimate can be shifted to almost any value simply by transitioning to a new parameterization of the model that is equivalent to the previous one but connected by a nonlinear transformation (Neal, 1996).

In our case of solving the inverse problem, we selected a total sample size of $S = 5000$. This choice was determined through a trial-and-error process, involving the examination of various sample sizes, beginning with 500.

2.7. *Markov Chain Monte Carlo methods*

Markov Chain Monte Carlo (MCMC) methods are a class of algorithms used to sample from probability distributions where direct sampling is difficult. A detailed discussion of the MCMC algorithm and its related methods is beyond the scope of this paper. However, we will briefly mention some of the most commonly used methods within this class of algorithms: Metropolis–Hastings (MH) (Metropolis et al., 1953; Hastings, 1970), Gibbs sampling (Geman and Geman, 1984), Hamiltonian Monte Carlo (HMC) (Duane et al., 1987), No-U-Turn Sampler (NUTS) (Hoffman and Gelman, 2014), slice sampling, Adaptive MCMC, Reversible Jump MCMC (RJMCMC) (Green, 1995), Sequential Monte Carlo (SMC) (Gordon et al., 1993), Multiple-Try Metropolis (MTM) (Liu and Chen, 1998), and Pseudo-Marginal MCMC (Beaumont, 2003). Among the mentioned methods, Metropolis–Hasting's sampling was chosen, for its simplicity in both application and implementation.

Due to the high dimensionality of the inverse problem and the time-consuming nature of the proposed RPT when employing MCMC methods for the entire dataset, a full-scale application is impractical. Instead, we select points from different microfacies, where permeability values are relatively high and where experimental values are available for one of these depths. The selected depths are 2885 m, no experimental value is available, but the estimated value is about 0.05 mD, and microfacies code: MF1; 2939 m, with experimental permeability equal 1.1 mD, and microfacies code: MF9 and 2981 m, no experimental value is available, but the estimated value is about 0.06 mD, and microfacies code: MF10. For these points, we perform inversion using Metropolis–Hasting's sampling to validate the results obtained through variational Bayes inversion.

To prevent divergence and reduce the time required for the sequential operations necessary to accurately sample from the posterior distribution, we begin with the maximum a posteriori estimate, similar to the approach used in FFVB inversion. The priors and likelihoods for the sampling method are identical to those in the variational Bayes approach.

To compare the results obtained from FFVB and Metropolis–Hastings sampling, we analyze the distributions distance for each parameter using Kullback–Leibler divergence (Kullback and Leibler, 1951).

$$D_{\mathrm{KL}} = \sum_{i\in N} P(x_i) \times \ln\frac{P(x_i)}{Q(x_i)} \tag{33}$$

where x_i is a member from the data set $\mathbf{X}$. Kullback–Leibler divergence is a measure of statistical distance that quantifies how one probability distribution P diverges from a reference probability distribution Q. In this context, the reference probability distribution is the one obtained from Metropolis–Hastings sampling.

3. Results

3.1. *Geological description of the studied formation—microfacies and sedimentary environment*

The Ilam Formation, approximately 130 m thick in Well A, comprises shallow marine limestones from the Santonian epoch and deeper marine shales from the Gurpi Formation. Detailed petrographic analysis of 440 thin sections from core samples and cuttings revealed various microfacies, categorized using the Dunham classification and methods by Flügel (2004) and Wilson

(1975). Key microfacies include ooid grainstone, peloid grainstone, and peloidal bioclast packstone, indicative of a high-energy, shallow marine environment, as well as pelagic gastropod wackestone, echinoid bioclast packstone, and radiolarian wackestone, associated with deeper marine settings. These findings, along with frequency diagrams and a sedimentary model for Well A, are presented in the *supplementary information file* for further reference (see Figs. SI1–SI4).

3.2. *Gas porosity and permeability measurements*

The analysis involved the measurement of porosity and permeability in 25 rock samples obtained from depths ranging from 2939.034 to 2975.61 m. The automated system “AP-608,” manufactured by Coretest Systems and depicted in Fig. 2, was employed for this purpose. Standard plugs, represented by cylindrical samples with dimensions of 30 mm in length and diameter, served as the testing medium. Nitrogen was utilized as the operational gas. Geometric characteristics were ascertained using a calliper, with 3–5 measurements taken at different locations on each sample to enhance the accuracy of volume calculations. Recorded data were meticulously documented. The recorded discrepancies in measurements were found to be within the acceptable limits specified in the terms of reference. Porosity measurement using the gas-volumetric method was grounded in Boyle-Mariotte law principles, where alterations in gas volumes and pressure facilitated the determination of sample volume and porosity. The absolute gas permeability values served as indicators of the rock's filtration properties. Detailed specifications for the gas permeability and effective porosity tester (Coretest Systems AP-608) are provided in Table 1. The results of the effective porosity and permeability corrected for Klingenberg are provided in Table 2. The study adhered to the non-stationary gas filtration method, employing nitrogen. The sample was positioned within the core holder of the “AP-608" system, with the sample's side surface being compressed by a rubber cuff under a pressure of 40 MPa. The confined pressure value represents the average effective pressure within the examined depth range. It is important to note that the assumption of a normal pore pressure gradient is a simplification made due to the absence of any engineering efforts aimed at accurately measuring the pore pressure in the well under investigation. While acknowledging the rough nature of this assumption, it should be underscored that no specific engineering endeavors were undertaken to conduct a precise measurement of the pore pressure in the well under study. This compression aimed to prevent air leakage between the side surface of the sample and the cuff.

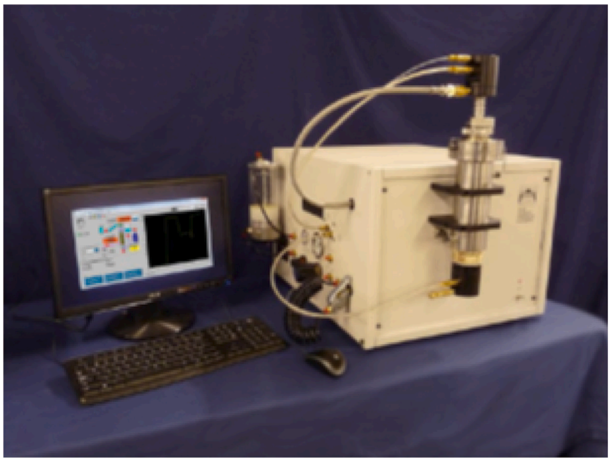

Fig. 2. Automated system for measuring porosity and permeability “AP-608” manufactured by Coretest Systems.

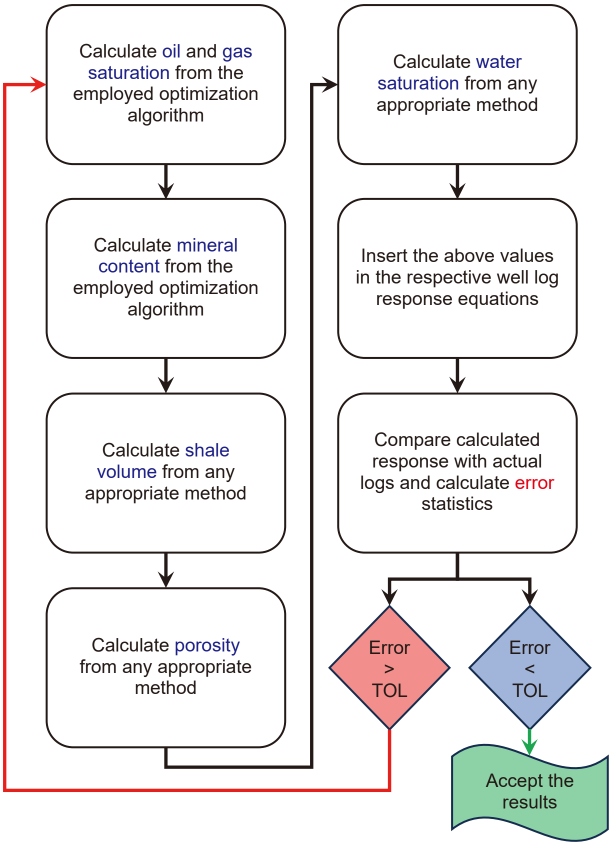

Fig. 3. Schematic representation of the algorithm used to well log data interpretation and petrophysical properties estimation. Here TOL represents the predefined tolerance for the optimization algorithm to be stopped.

3.3. *Available well log data and the interpretation results*

In the present investigation, a comprehensive set of well log data acquired within the depth range of 2870.0–3008.8 m, with a measurement interval of 15.24 cm, has been furnished. The graphical representation of these data is depicted in Fig. 4. In the aforementioned figures, the acronyms CALI, DRHO, DT, GKUT, GRKT, NPHI, PE, RHOB, RT, RXO correspond to the caliper log, neutron density correction, P-wave interval time, total potassium, uranium and thorium gamma rays measured by spectral gamma log, potassium to thorium ratio, neutron porosity, photoelectric effect, bulk density, deep and shallow resistivities, respectively. The determination of calcite volume, alongside oil and gas saturations, as well as other pertinent petrophysical properties, is conducted utilizing the iterative algorithm delineated in the methodology section and depicted in Fig. 3. Fig. 5 illustrates the interpreted well log data obtained through the aforementioned methodologies and procedures. Figs. 4 and 5 are prepared by Corel software.

3.4. *Inversion results*

The forward problem yields seismic velocity and true formation electrical resistivity, while the inverse problem is solved using the

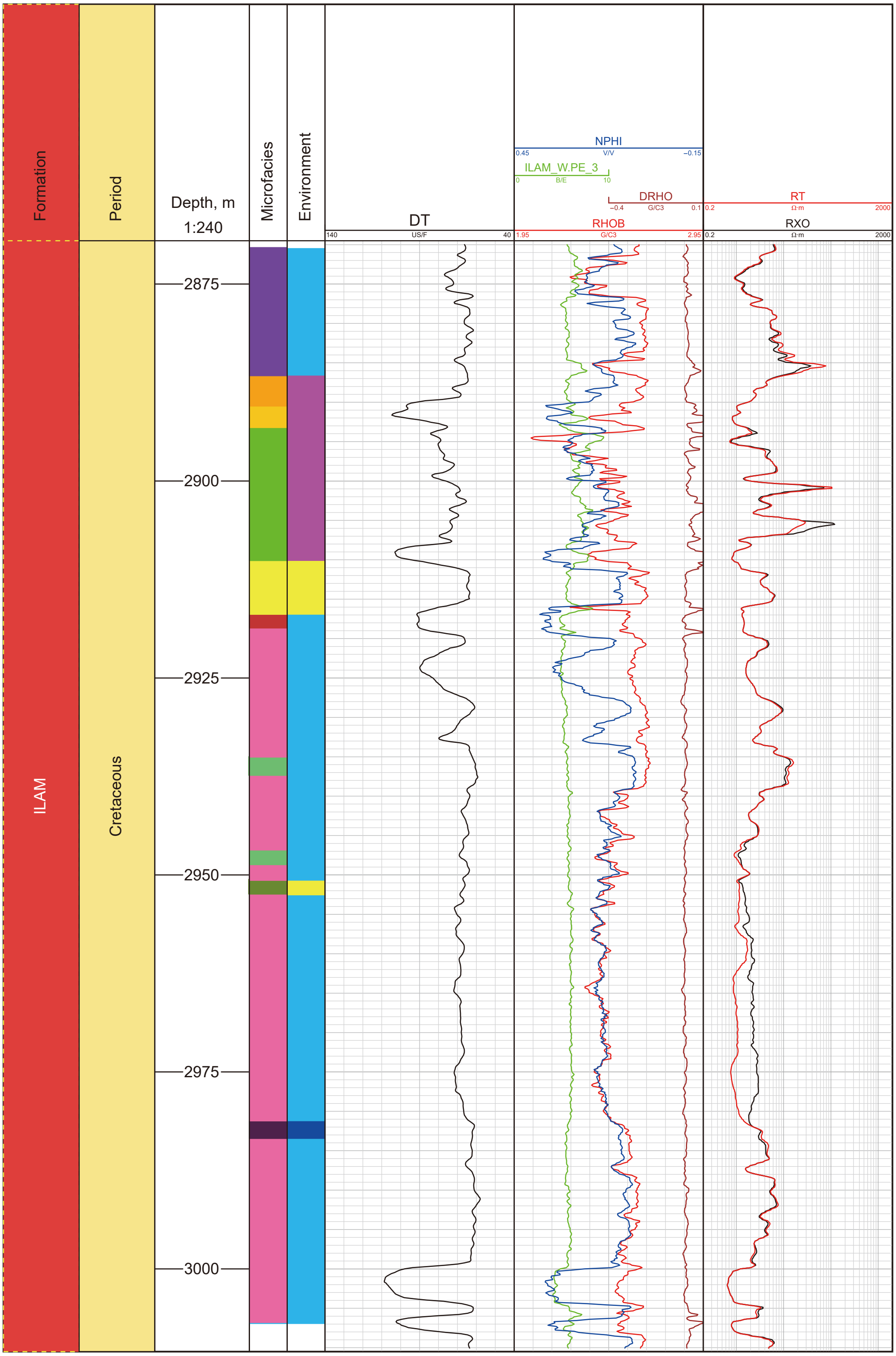

Fig. 4. Full set of well log data provided for the studied well.

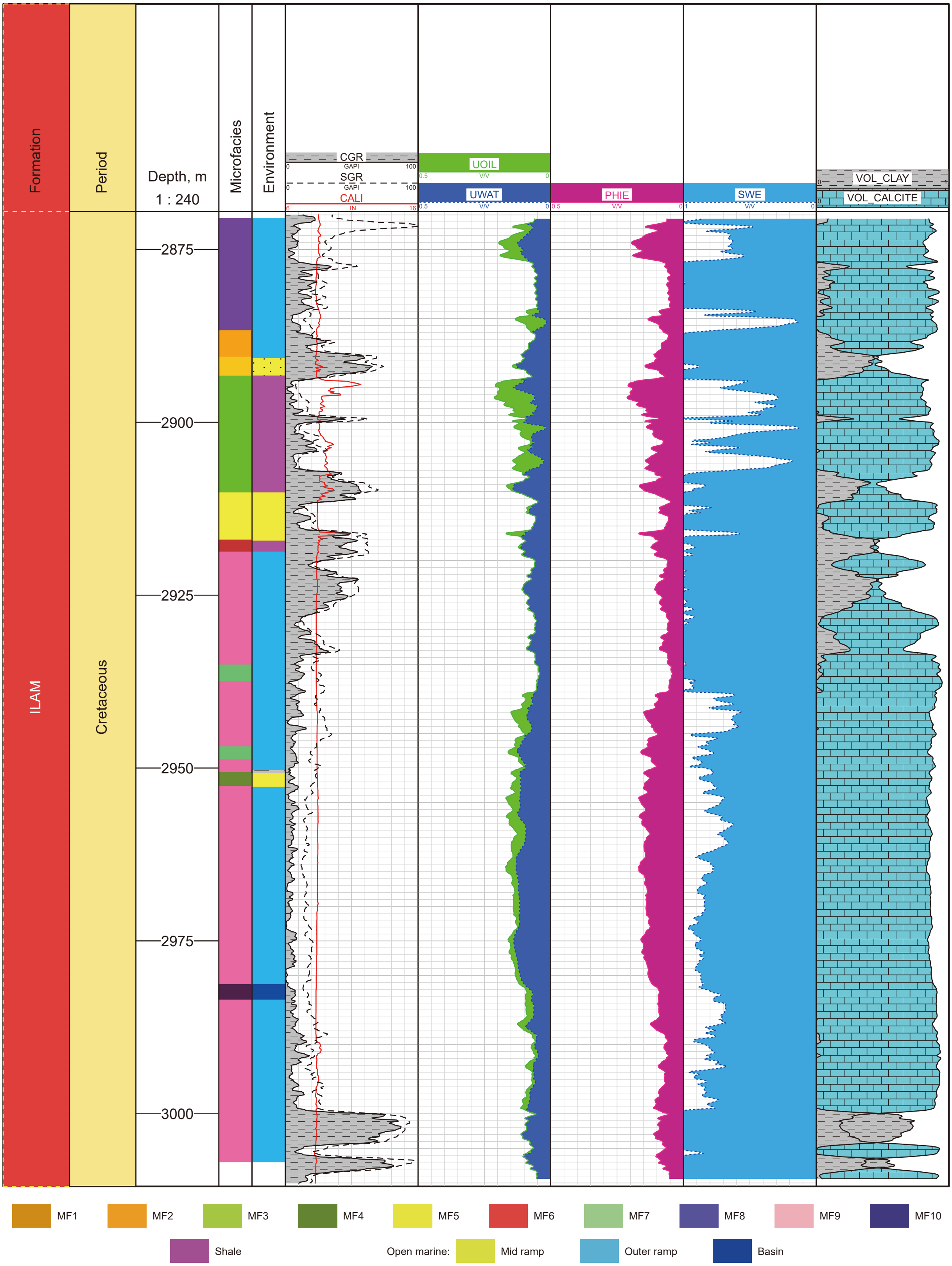

Fig. 5. Results of interpretation of well log data.

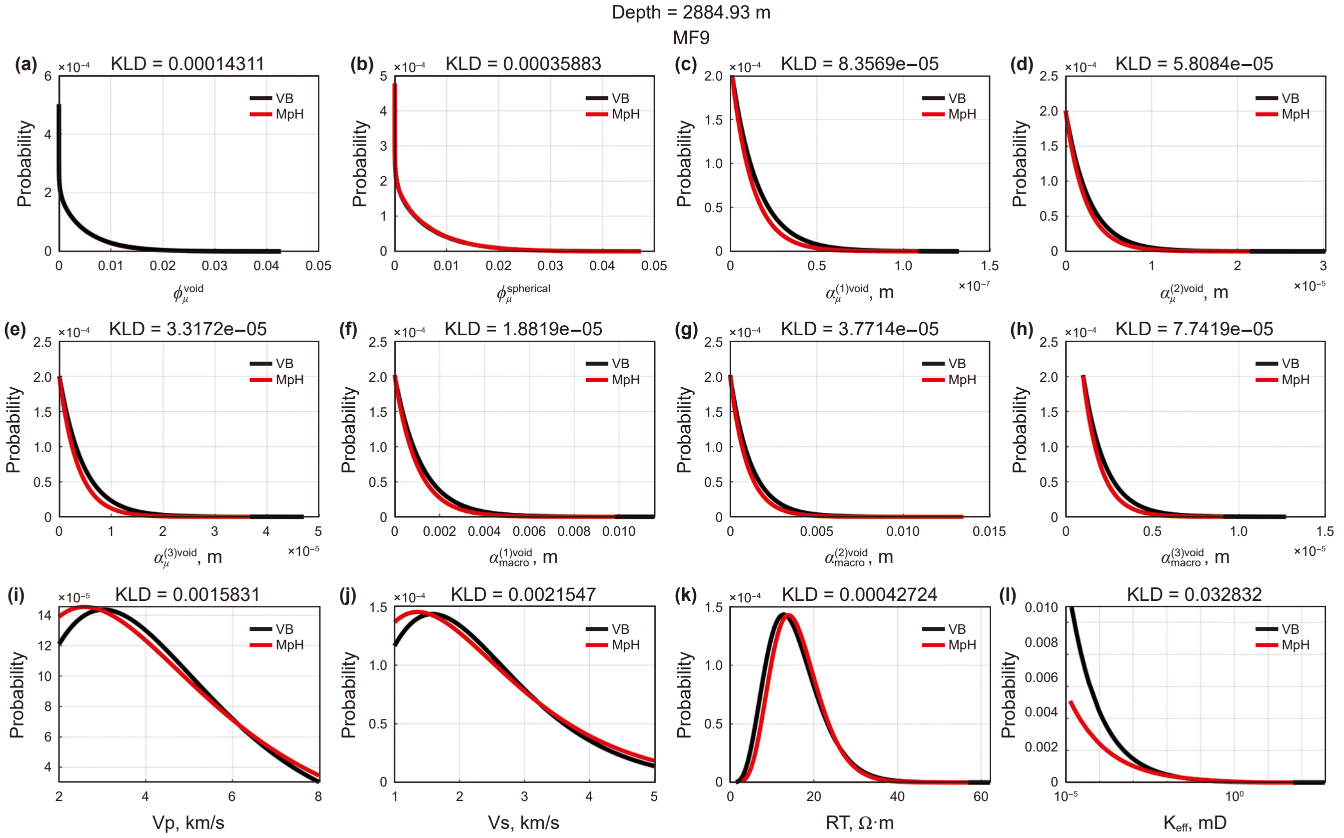

Fig. 6. The probability distributions generated as the result of FFVI (black lines) and MH sampling (red lines) at the depth of 2885.0 m, with microfacies code: MF1, for **(a)–(h)** model parameters and **(i)–(j)** estimated P-wave and S-wave travel times, **(k)** true formation resistivity and **(l)** hydraulic permeability. The Kullback Leibler divergence is represented by KLD on top of each figure for the respective PDFs. Vp demotes P-wave velocity, Vs denotes S-wave velocity.

variational Bayes approach, providing computational efficiency, scalability, and handling uncertainty. VB excels in its ability to approximate complex posterior distributions with tractable computations, thus mitigating the computational burden often associated with parameter estimation in complex probabilistic models. Unlike MCMC, which relies on iterative sampling techniques that can be computationally intensive, VB offers a more streamlined approach by optimizing a tractable variational approximation to the true posterior distribution (Nawaz et al., 2020; Zhang et al., 2021).

Variational Bayes (VB) enables the derivation of probability distributions for parameters, yielding a collection of data points with associated probabilities. The median is favored for skewed distributions due to its robustness to outliers, reflecting central position, and balancing skewed tails. In our scenario, the structural parameters, modeled as a beta distribution, lead us to prefer the median over the mean for a more probable value.

To clarify the results and ensure consistency in depicting them on a well log data scale, we have provided a *supplementary information file*. This file contains figures plotted in well log scale, using Techlog, a specialized petrophysical software, where the uncertainties associated with the estimated and reconstructed parameters are presented by upper and lower confidence intervals, as described in the supplementary information. This approach aims to enhance the clarity and reliability of the presented data.

Figs. 6–8 show the probability density functions for the model parameters, compressional and shear wave velocities, electrical resistivity, and hydraulic permeability, at depths of 2885, 2981 and 2939 m with microfacies code MF1, MF10 and MF9 respectively. The black line represents the FFVB results, and the red line represents the MH sampling results. We extracted 10,000 samples from the posterior distributions around the maximum a posteriori point obtained similarly for the FFVB approach. The acceptance ratio of the sampling was about 0.6 and computational time of the employed multi-cluster multi-thread processor was about 72 h for the three depths. The Kullback-Leibler divergence values, indicated on top of each figure, indicates that the distance between the estimated probabilities from FFVB and the fitted probabilities from MH sampling is quite small, demonstrating the effectiveness of the FFVB inversion.

A comprehensive discussion on necessity of including uncertainty in subsurface-property estimation from remote geophysical measurements is provided in Bosch et al. (2010) and Zhang et al. (2021).

Fig. 9 (see Fig. SI5 to show the results and the associated uncertainty in well log data scale) illustrates the probability density function of P-wave velocities (a) (see also Fig. SI5(a)) and true formation resistivity values (b) (see also Fig. SI5(b)), with probability values represented by colors. The black line denotes the measured P-wave and resistivity values. In both cases, the actual (measured) values fall within the high probability zones of the estimated density functions, indicating the success of the inversion operation for both P-wave velocities and true resistivity values. Predicted permeability values are also depicted through their respective probability distribution functions, with the black line representing the median. Red filled markers indicate laboratory-measured permeability values under approximate reservoir conditions, as detailed in the previous section (refer to Fig. 9(c) and Fig. SI5(c)).

Fig. 10 (see Fig. SI6 to show the results and the associated uncertainty in well log data scale) showcases both total micro-

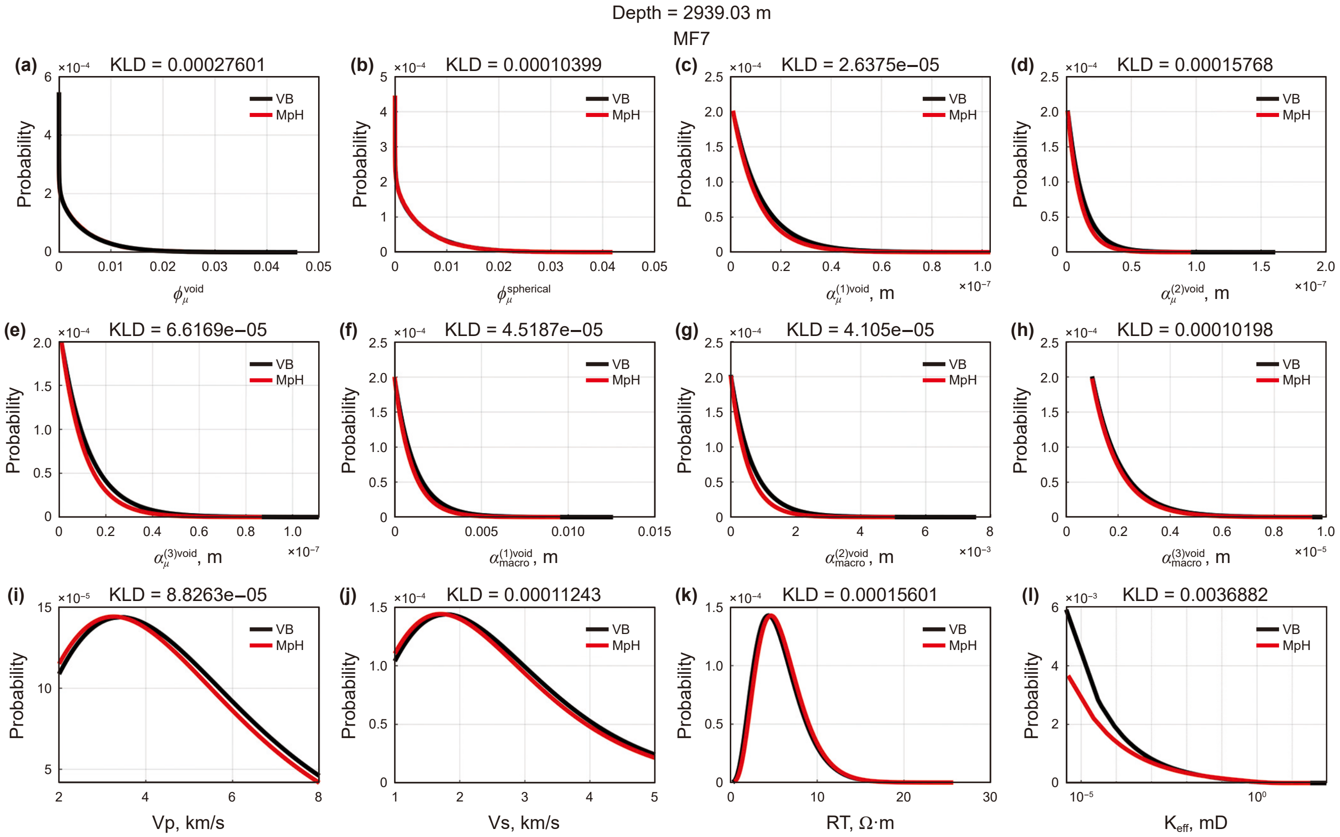

Fig. 7. The probability distributions generated as the result of FFVI (black lines) and MH sampling (red lines) at the depth of 2939.0 m, with microfacies code: MF9, for **(a)–(h)** model parameters and **(i)–(j)** estimated P-wave and S-wave travel times, **(k)** true formation resistivity and **(l)** hydraulic permeability. The Kullback Leibler divergence is represented by KLD on top of each figure for the respective PDFs.

porosity (red line, comprising micro-voids porosity and micro-spherical pores porosity) and macro-void porosity (black line, total porosity minus total micro-porosity) as well as permeability prediction results. The results presented in Fig. 10 demonstrate a strong alignment between the inversion results for micro-porosities and permeability values and the geological evidence from the earlier microfacies analysis. This figure illustrates the inverse problem solution for the probability density function of micro void porosity (Fig. 10(a)), the probability density function of micro spherical pore porosity (Fig. 10(b)), and both macro void porosity (the black line) and total micro porosity (the red line in Fig. 10(c)) as well as (Fig. 10(d)) permeability. The colors indicate probability, with the most probable values shown in red, transitioning to blue for lower probabilities. A colormap is included to clarify the meaning of the colors. In Fig. 10, from 2870 to 2886 m, Rotalida Mudstone to Wackestone (MF8) is evident, where the fine-grained mudstone nature increases microporosity, while weak dolomitization and vug-type porosities contribute to an overall increase in macro-porosity and permeability. The effective porosity falls within the range of 6%–21%, consistent with the high permeability obtained from inversion (see Fig. 5 for well log data interpretation results). From 2886 to 2890 m, Ooid Grainstone (MF1) is present, exhibiting a grain-supported texture with radial ooids, suggesting good primary porosity. However, the high degree of cementation is the main factor reducing permeability, resulting in low reservoir quality for this section. The effective porosity deduced from well log data barely reaches 7% (see Fig. 5 for well log data interpretation results). From 2890 to 2893.5 m, Peloid Grainstone (MF2) is observed, with good macro-porosity expected from the presence of peloids. Well log data interpretation depicts relatively high effective porosity from 0.9% to ~16%, and permeability values for this thin depth interval are in good consistency with the fluctuation in effective porosity.

Continuing from 2893.5 to 2909 m, Peloidal Bioclast Packstone (MF3) is encountered, where a high microporosity value is expected due to the presence of mud and cement. The obtained micro-porosity aligns with observed geological thin sections, and effective porosity remains similar to the previous depth interval. The respective permeability fluctuates according to the effective porosity values. Moving to the next depth interval, from 2909 to 2917 m, the observed microfacies is Echinoids Bioclast Packstone (MF5), characterized by a more mud-supported interval. Consequently, high micro-porosity is expected and obtained from inversion. Due to mud-supported sections, effective porosity is relatively low (ranging from 0.7% to 5%), resulting in low permeability values. The subsequent depth interval, from 2917 to 2918 m, reveals Sponge Spicules Calsispherolide Mudstone (MF6), where the mud matrix is the primary reason for high microporosity observed in inversion results. Effective porosity is extremely low (<2%), consistent with zero permeability obtained from inversion in this section.

From 2918 to 2935 m, 2937 to 2947 m, 2948 to 2951 m, 2952.1 to 2982 m, and 2983.1 to 3000 m, the main microfacies of the Ilam Formation-Calsispherolide Wackestone to Packstone (MF9) are present. Micro-porosity values are high due to the mud matrix, and effective porosity for these intervals ranges from 2% to 20%, satisfying the high permeability obtained from both core sample analysis and inversion results. Thin section studies reveal dolomitization and pyritization, contributing to increased effective porosity and permeability values. Dolomitization is expected to result in high

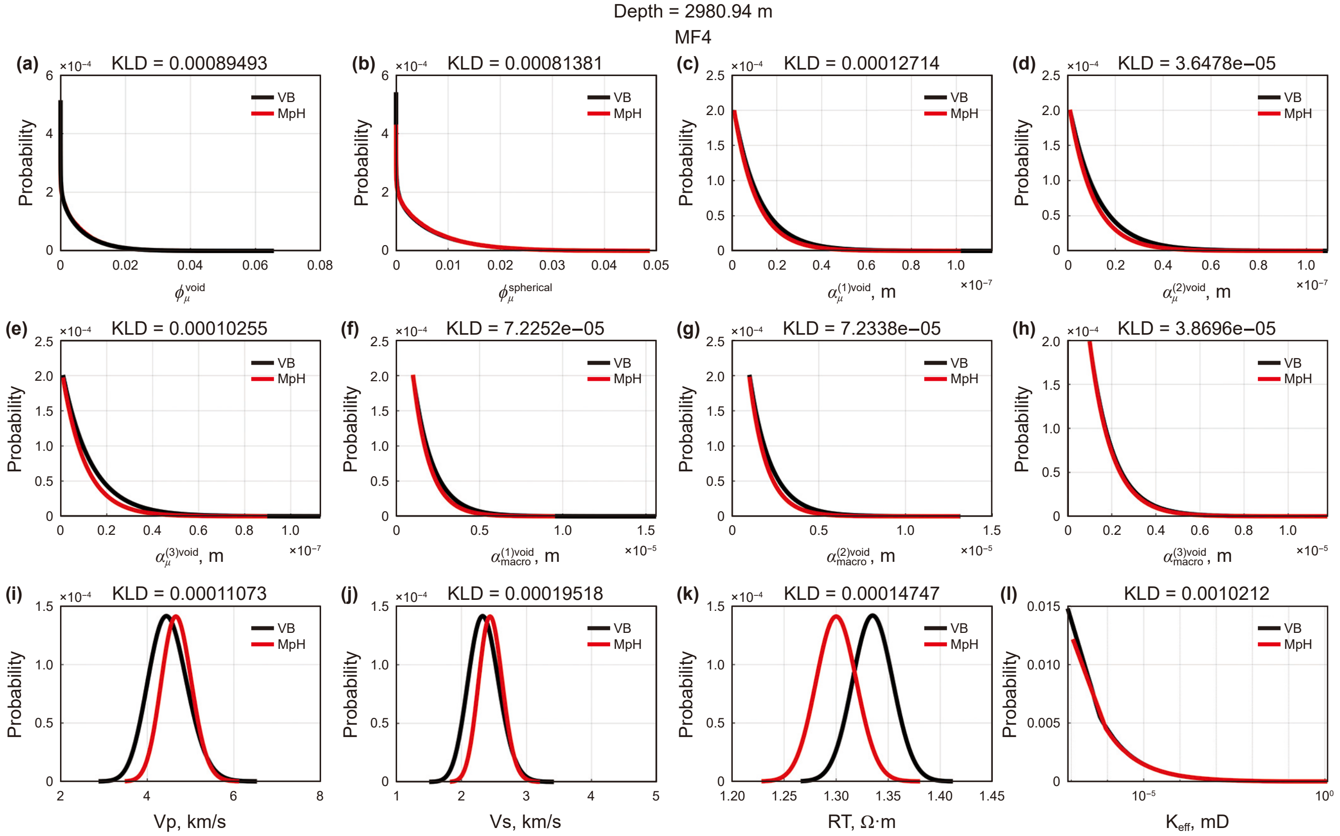

Fig. 8. The probability distributions generated as the result of FFVI (black lines) and MH sampling (red lines) at the depth of 2981.0 m, with microfacies code: MF10, for **(a)–(h)** model parameters and **(i)–(j)** estimated P-wave and S-wave travel times, **(k)** true formation resistivity and **(l)** hydraulic permeability. The Kullback Leibler divergence is represented by KLD on top of each figure for the respective PDFs.

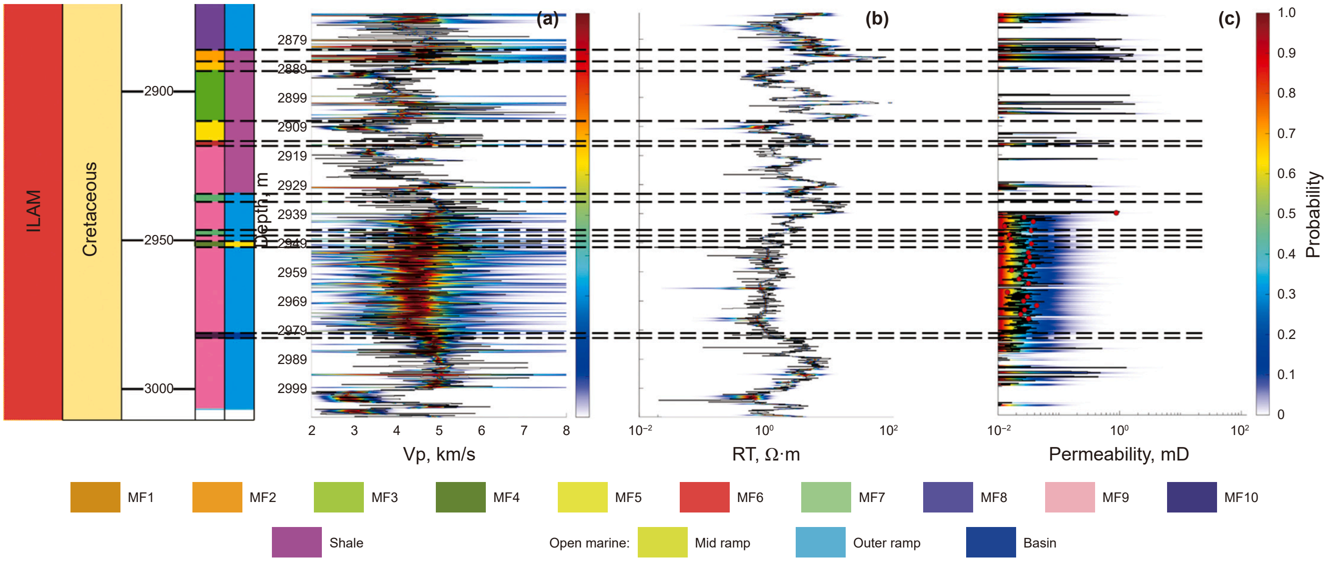

Fig. 9. Results of direct problem solution to estimate **(a)** the probability density function of P-wave velocity (the colour plot), and the actual measured P-wave velocity, obtained from well log data (the black line), **(b)** the probability density function of true formation resistivity (the colour plot), and the actual measured true formation resistivity, obtained from well log data (the black line), and **(c)** the probability density function of permeability (the colour plot), the median of the probability density functions (the black line) and the measured in laboratory permeability values (the red markers).

values of intercrystalline micro-porosity, serving as the second reason for the observed high micro-porosities and permeabilities from inversion. From 2935.1 to 2937 m and 2947.1 to 2948 m, Planktonic Foraminifera Packstone (MF7) is present, with the presence of micrite increasing microporosity, consistent with the high microporosities observed from inversion. Effective porosity values are about 3%–4%, indicating the presence of permeability evident from the inversion results depicted in Fig. 9(c).

Table 1
Technical characteristics of the Coretest Systems AP-608 system for determining gas permeability and effective porosity in reservoir conditions.

Feature	Value
Gas permeability measurement range, mD	0.001–10000
Measurement range of effective porosity, %	0.1–40
Diameter range of the samples, mm	27–33
Length range of the samples, mm	25–101
Sample pressure range, atm	500–9500
Limits of acceptable error limit for gas permeability, %	8
Limits of acceptable error limit for porosity, %	6
Limits of the relative standard deviation of the random component of the acceptable error limit of effective porosity, %	3

From 2951.1 to 2952 m, Pelagic Gastropode Wackestone (MF4) is observed, where the mud matrix is the main reason for high micro-porosity. Effective porosity values range from 13% to 15%, and respective permeability values obtained from core analysis and inversion are high, similar to the MF9 sections. While the depth interval is not thick on its own, it is located between MF9 depth intervals, contributing to a good reservoir section. From 2982 to 2983 m, Radiolarian Wackestone, characterized by a mud matrix with high micro-porosities, is present. Effective porosity values are lower than MF9 and MF4, ranging from 8% to 9%, and permeability values are consequently lower than the mentioned sections but higher than other microfacies sections.

Examining the microfacies characterized by relatively high permeability values allows us to infer that the microfacies within the outer ramp sedimentary environment demonstrate comparatively elevated microporosity and permeability values. The fine-grained nature of sediments in the outer ramp facilitates the creation of abundant micropores, contributing to higher microporosity values. Additionally, the relatively low energy environment limits compaction, preserving these small-scale pores and further enhancing microporosity. The heightened permeability observed in the outer ramp can be attributed to the processes of dolomitization and pyritization that occur within this sedimentary environment.

Figs. 11 and 12 represent the inversion result for semi-axis of the voids, which are assumed to be in form of general ellipsoids, in micro (Fig. SI7(a)–(c)) and macro scales (Fig. SI7(d)–(f)). Again, here we obtained the probability density functions for these semi-axes and the probability values are depicted in form of colors.

Since in rock physics modelling the concept of aspect ratio – $AR_1 = \alpha_2/\alpha_1$ and $AR_2 = \alpha_3/\alpha_1$, where the AR_1, AR_2, α_1, α_2, α_3 are

Table 2
Absolute Klinkenberg-corrected permeability and effective porosity by gas volumetric method.

Sample	Length, cm	Diam, cm	V bulk, cm^3	Weight, gr	P conf, MPa	V pore, cm^3	Porosity	K air, mD	K klink, mD
B11-14/1	3.025	2.982	21.123	53.220	40.10	2.220	10.51	1.126	1.0900
B11-14/2	2.561	2.972	17.763	44.595	40.11	1.178	6.63	0.063	0.0157
B11-14/3	2.665	2.977	18.547	45.817	40.12	2.250	12.13	0.042	0.0240
B5-8/1	2.965	2.979	20.666	54.692	40.11	2.738	13.25	0.050	0.0183
B5-8/2	2.841	2.980	19.822	52.320	39.98	2.085	10.52	0.108	0.0296
B5-8/3	3.034	2.978	21.133	55.581	40.10	4.339	20.53	0.119	0.0186
B6-5/1	3.011	2.972	20.892	54.536	39.99	2.460	11.77	0.020	0.0120
B6-5/2	3.022	2.980	21.081	54.450	40.13	3.663	17.38	0.085	0.0263
M2-16/1	3.036	2.976	21.118	50.430	40.05	2.634	12.47	0.083	0.0154
M2-16/2	3.014	2.978	20.993	51.143	40.03	3.801	18.11	0.108	0.0288
M4-8/2	2.909	2.959	20.004	36.349	39.97	2.680	13.40	0.090	0.0344
M4-8/3	2.910	2.953	19.930	48.096	39.99	3.917	19.66	0.096	0.0203
M4-8/4	2.959	2.961	20.379	48.949	40.00	3.368	16.53	0.030	0.0136
M4-2/1	3.047	2.990	21.395	51.740	40.00	2.569	12.01	0.110	0.0201
M4-2/2	2.872	2.990	20.173	48.623	40.17	3.395	16.83	0.095	0.0366
M4-2/3	3.039	2.990	21.338	51.713	40.16	2.880	13.49	0.101	0.0164
M4-2/4	2.945	2.988	20.654	48.805	40.09	4.486	21.72	0.088	0.0554
M4-2/5	3.015	2.987	21.117	53.631	40.09	2.859	13.54	0.098	0.0000
M4-2/6	3.012	2.986	21.082	53.741	40.10	2.565	12.17	0.121	0.0292
M4-2/7	2.990	2.971	20.718	54.213	40.10	3.825	18.46	0.118	0.0254
M4-2/8	2.851	2.990	20.008	54.111	39.97	3.725	18.62	0.026	0.0182
M4-2/9	2.985	2.899	19.693	52.366	39.98	2.308	11.72	0.064	0.0299
M4-2/10	3.015	2.956	20.681	54.612	40.12	1.225	5.93	0.104	0.0204
M4-2/11	3.014	2.984	21.067	55.491	40.11	3.207	15.22	0.076	0.0375
M4-2/12	3.022	2.963	20.827	48.953	40.12	3.978	19.10	0.116	0.0259

Table 3
The model parameters and their respective prior distribution details.

Parameter	Prior type	Shape factor ($\boldsymbol{\alpha}$)	Scale factor ($\boldsymbol{\beta}$)	Mean ($\boldsymbol{\mu}$)	Standard deviation ($\boldsymbol{\sigma}$)
Compressional wave velocity sampling noise	Inverse Gamma	4	0.2	~0.07	~0.05
True formation resistivity sampling noise	Inverse Gamma	4	0.2	~0.07	~0.05
Micro voids porosity $\phi_{\text{micro}}^{\text{void}}$	Beta	$0.5(1-\phi/2)/(\phi/2)$	0.5	–	–
Micro spherical pores porosity $\phi_{\text{micro}}^{\text{pore}}$	Beta	$0.5(1-\phi/2)/(\phi/2)$	0.5	–	–
Microvoids semi-axis in x_1 direction $\alpha_{\text{micro}}^{(1)\text{void}}$	Beta	5×10^6	0.5	~10^{-7}	~2×10^{-7}
Microvoids semi-axis in x_2 direction $\alpha_{\text{micro}}^{(2)\text{void}}$	Beta	5×10^6	0.5	~10^{-7}	~2×10^{-7}
Microvoids semi-axis in x_3 direction $\alpha_{\text{micro}}^{(3)\text{void}}$	Beta	5×10^6	0.5	~10^{-7}	~2×10^{-7}
Macrovoids semi-axis in x_1 direction $\alpha_{\text{macro}}^{(1)\text{void}}$	Beta	5×10^3	0.5	~10^{-4}	2×10^{-4}
Macrovoids semi-axis in x_2 direction $\alpha_{\text{macro}}^{(2)\text{void}}$	Beta	5×10^3	0.5	10^{-4}	2×10^{-4}
Macrovoids semi-axis in x_3 direction $\alpha_{\text{macro}}^{(3)\text{void}}$	Beta	5×10^3	0.5	10^{-4}	2×10^{-4}

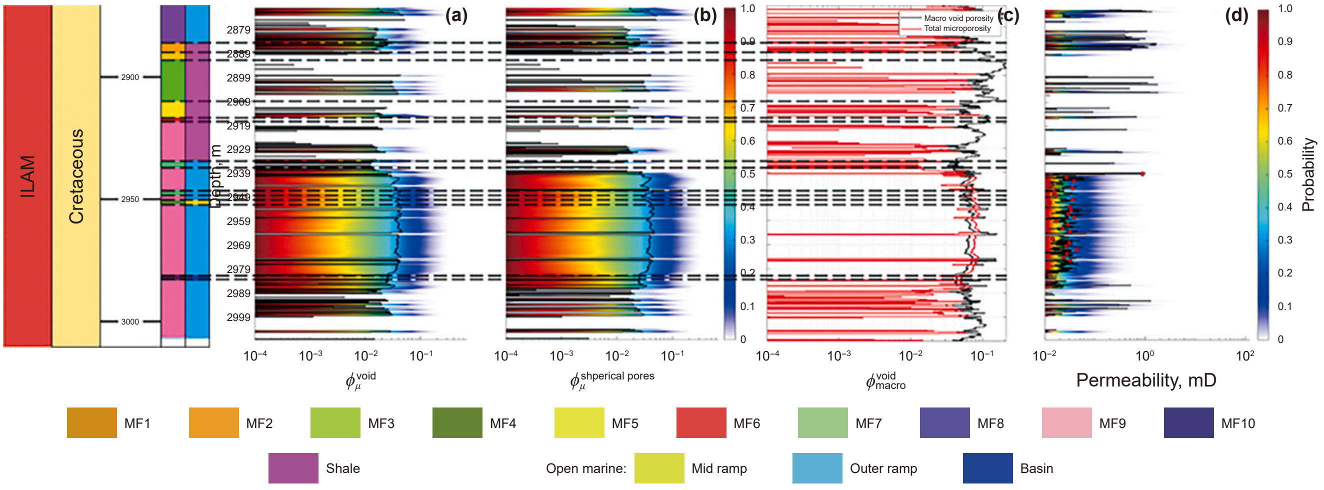

Fig. 10. Results of inverse problem solution for **(a)** probability density function of micro void porosity, **(b)** probability density function of micro spherical pores porosity, and **(c)** macro voids porosity (the black line). Red line in (c) represents the total micro porosity. **(d)** The mean estimated (black line) and measured permeability values (red markers).

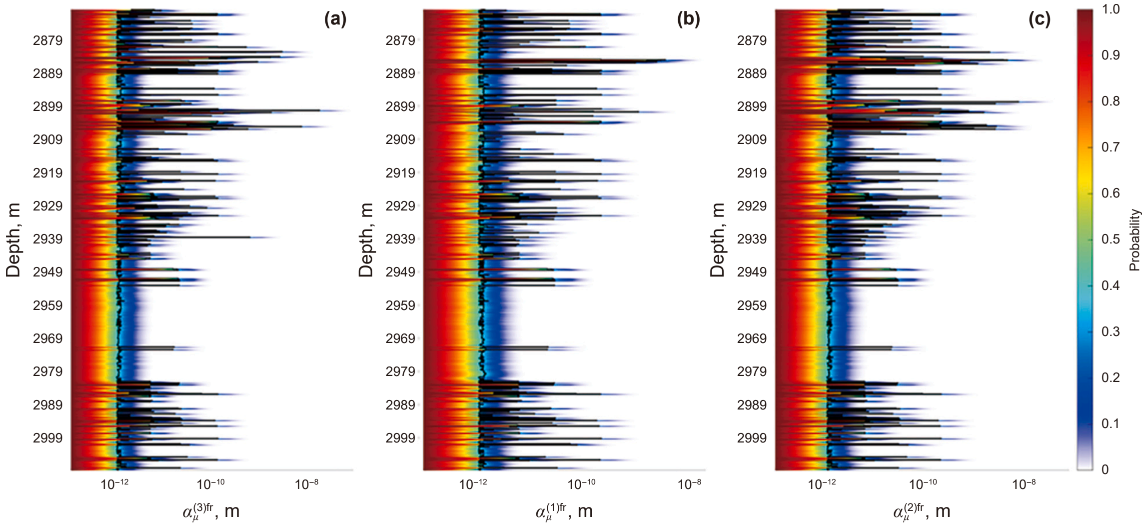

Fig. 11. Inversion results for probability density function of semi axis of micro voids aligns in **(a)** *x*1, **(b)** *x*2 and **(c)** *x*3 directions (the colour plot), and their respective median (the black line).

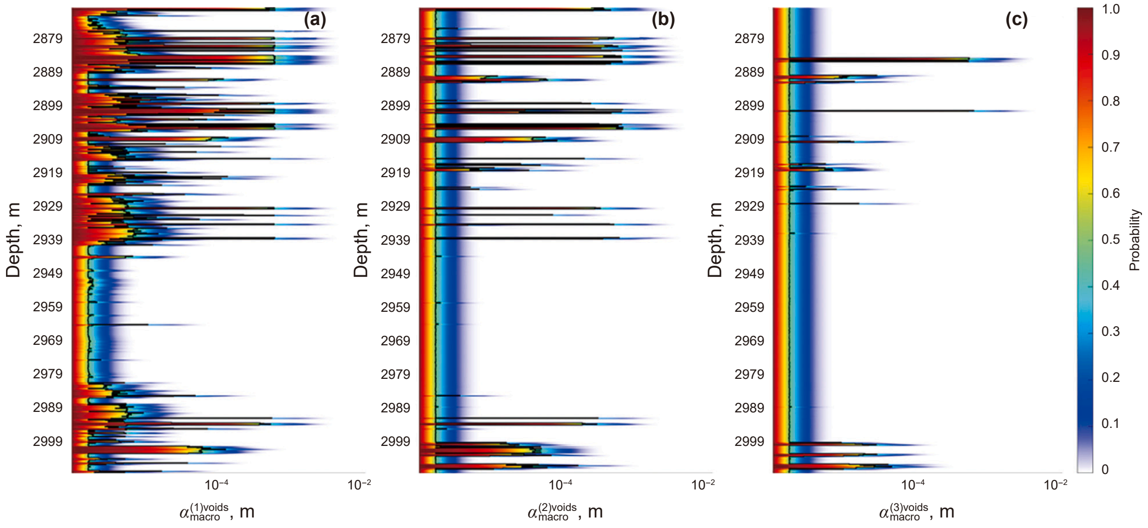

Fig. 12. Inversion results for probability density function of semi axis of macro voids aligns in **(a)** *x*1, **(b)** *x*2 and **(c)** *x*3 directions (the colour plot), and their respective median (the black line).

first and second aspect ratio, semi axis's align with x_1, x_2 and x_3 axis of cartesian coordinate axis respectively, is more familiar we represent the aspect ratio values obtained by dividing the median of the probability density functions of the semi – axes in Figs. 11 and 12(a)–(c) (Fig. SI7(a)–(c)). For clarity and familiarity, we present the aspect ratio values obtained by dividing the median of the probability density functions of the semi-axes in Fig. SI8. As depicted in Fig. SI 8(a) and (b) the micro-voids exhibit a tendency towards a penny-shaped ellipsoidal morphology, while the results presented in Fig. SI 8(c) and (d) indicate that macro-voids exhibit a needle-shaped morphology. In high-permeability zones, the pores tend to be more spherical.

Justifying the morphological characteristics of the voids faces practical challenges due to the following reasons: 1) Assumption of general ellipsoids: The obtained semi-axis values for voids are based on the rough assumption of considering the voids as general three-dimensional ellipsoids. This assumption may not accurately represent the actual morphological complexity of voids in many cases. Despite its simplicity, this approach facilitates methods such as effective medium theory. 2) Limitations of equipment for void characterization: Comprehensive characterization of the morphological characteristics of voids requires a three-dimensional micro tomographic scanner. However, even if such a device is available, it may face limitations in monitoring void morphology at microscales. Generating three-dimensional images from two-dimensional images obtained from scanning electron microscopy (SEM) might not be successful in the case of heterogeneous carbonates, where the complexity of the rock structure could impede accurate reconstruction. In summary, the challenges in justifying the morphological characteristics of voids stem from the inherent assumptions made during analysis and the limitations of current imaging technologies, particularly in capturing the intricate features of micro- and macro-voids in heterogeneous carbonate formations.

Again, we emphasize that Figs. 9–12 were created using a combination of MatLab and Corel, specifically in the microfacies and sedimentary environment section on the left side of the figures was prepared by Corel and the color plots were prepared by MatLab. As far as our knowledge extends, there is currently no commercially available software capable of generating color plots in a well log scale. The disparity in style between Figs. 3 and 4 compared to Figs. 9–12 arises from the distinct software utilized for their respective plotting processes. These figures are reconstructed in well log data scale, in another form, using Techlog software, in *supplementary information file*.

4. Discussion

4.1. Suitability of the proposed RPM for carbonate reservoirs pore complexity

The hierarchical methodology proposed builds upon well-established theoretical precedents in carbonate rock physics modeling. The conceptual framework of treating carbonate reservoirs as an ensemble of matrix blocks separated by fractures and vugs represents standard industry practice, as demonstrated by extensive literature documenting the dual-porosity dual-permeability nature of these systems (van Golf-Racht, 1982; DeGraff et al., 2005; Uba et al., 2007; Saidian et al., 2021). Carbonate reservoirs exhibit extraordinary pore structure complexity spanning multiple orders of magnitude in scale, from nanometer-scale microporosity within matrix blocks to meter-scale vugs and fractures. Carbonates also exhibit distinction between matrix microporosity (typically poorly connected) and fracture-vug networks (providing primary flow pathways) which is critical for accurate permeability prediction. The proposed two-stage approach effectively captures this multi-scale heterogeneity through: Stage 1 (Matrix Block Characterization): Models the intra-matrix microporosity system using ellipsoidal microvoids ($\alpha_1^{mic_r}$, $\alpha_2^{mic_r}$, $\alpha_3^{mic_r}$) combined with spherical micropores, representing the complex diagenetic porosity that dominates fluid storage in carbonate systems. This stage accounts for the typically tortuous, poorly connected microporosity that characterizes carbonate matrix blocks. Stage 2 (Inter-Block System Modeling): Incorporates the macro-scale fracture-vug network ($\alpha_1^{mac_r}$, $\alpha_2^{mac_r}$, $\alpha_3^{mac_r}$) that controls primary fluid flow pathways. This separation is geologically appropriate as it reflects the distinct formation mechanisms and flow characteristics of these pore systems (Nie et al., 2012; Mondal and Singh, 2024).

4.2. Impact of pore structure in different microfacies on permeability

Fig. 13 visualizes the impact of microfacies on effective porosity, permeability, effective porosity–permeability relation, and microporosity, and all estimated through the proposed FFVB inversion. Because of their low value, we normalized the permeability and microporosity values, and divided the normalized values into five scores, score 0 (zero permeability/microporosity) to score 5 (high permeability/microporosity). According to the obtained results presented in Fig. 13, the nine microfacies identified in the Ilam Formation demonstrate a complex relationship between pore structure characteristics and permeability that defies simple depositional texture-based predictions. The comprehensive analysis reveals that only two microfacies (MF1 and MF2) exhibit grain-supported textures, while seven microfacies (MF3-MF9) are mud-supported, yet the permeability distribution across these facies shows remarkable variability that highlights the critical role of diagenetic processes in overriding primary depositional controls. The grain-supported microfacies present contrasting reservoir quality outcomes despite sharing similar primary depositional characteristics. MF1 (ooid grainstone) demonstrates how intensive calcite cementation can completely negate the advantages of excellent primary framework porosity, reducing effective porosity to approximately 7% and permeability to low values. The radial ooid framework initially provides optimal interparticle pore space, but cement precipitation blocks critical pore throats and destroys connectivity pathways. In contrast, MF2 (peloid grainstone) maintains good reservoir quality with effective porosity ranging from 0.9% to 16% due to less intensive cementation, allowing preservation of both primary porosity and flow pathways through the peloid-supported framework. The mud-supported microfacies demonstrate the most significant variations in reservoir quality, ranging from zero permeability (MF6) to excellent permeability (MF4, MF8, MF9). This dramatic range illustrates how secondary diagenetic processes can either enhance or further degrade originally unfavorable depositional textures. MF6 (sponge spicules mudstone) represents the extreme case where mud matrix dominance creates abundant microporosity but extremely poor connectivity, resulting in effective porosity below 2% and zero permeability. The fine-grained nature creates numerous micropores within the mud matrix, but the absence of larger pore throats prevents effective fluid flow. Conversely, the high-performing mud-supported microfacies (MF4, MF8, MF9) demonstrate how specific diagenetic processes can transform poor primary textures into excellent reservoir intervals. MF4 (pelagic gastropode wackestone) achieves effective porosity of 13%–15% and high permeability through strategic location between high-quality MF9 intervals and weak dolomitization

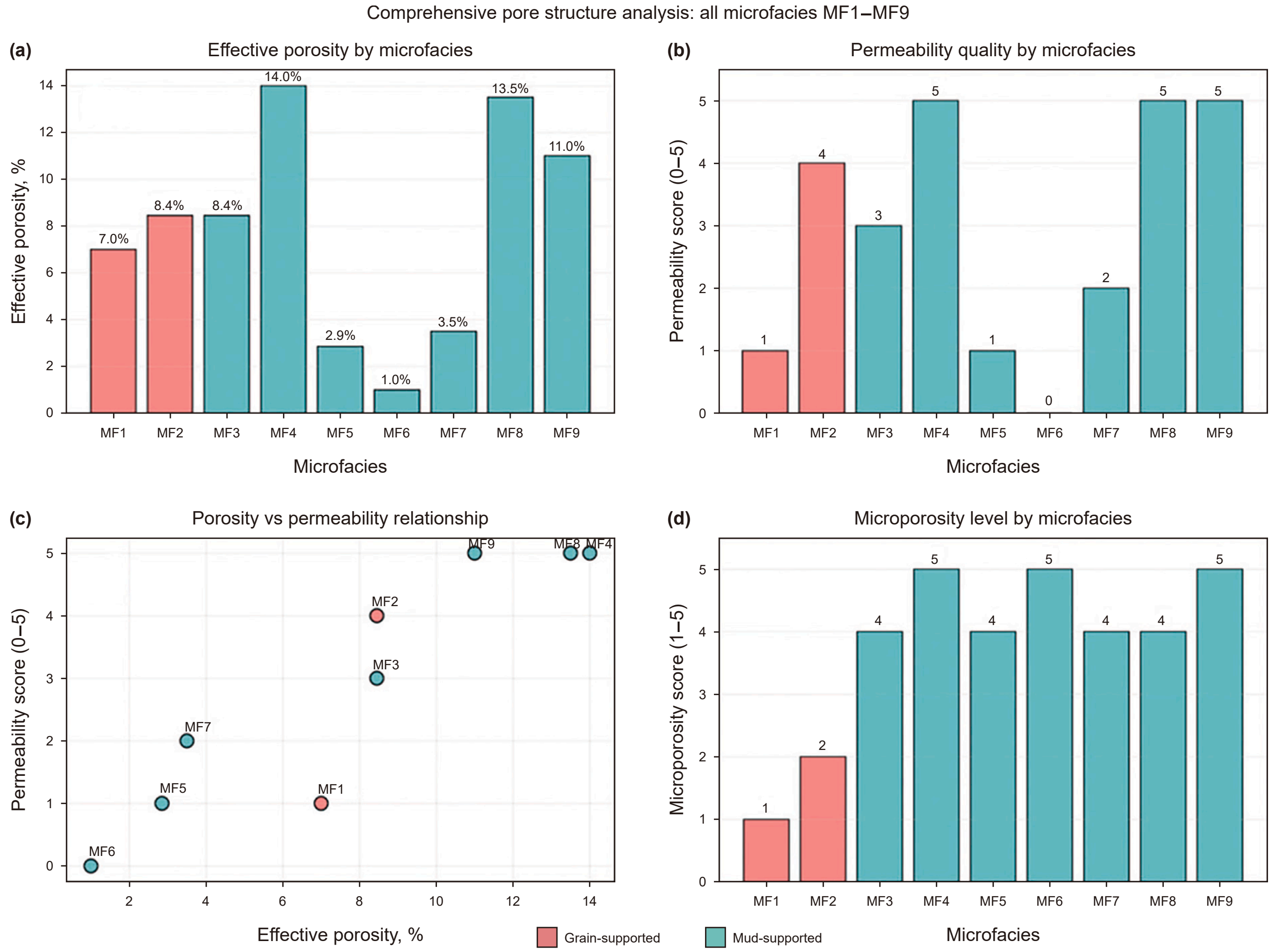

Fig. 13. Comprehensive pore structure analysis and its relation to permeability all estimated using the proposed FFVB inverison. **(a)** Effective porosity, **(b)** normalized permeability score, **(c)** normalized permeability score vs effective porosity, **(d)** normalized microporosity score for detected microfacies.

processes. MF8 (rotalida mudstone to wackestone) develops the highest effective porosity range (6%–21%) through the combination of weak dolomitization and vug-type dissolution porosity, creating a dual-porosity system with both micropore storage and macropore flow capacity. MF9 (calsispherolide wackestone to packstone) represents the most volumetrically significant microfacies and demonstrates the optimal combination of dolomitization and pyritization processes. These diagenetic modifications create intercrystalline porosity between dolomite rhombs while pyritization contributes additional porosity through mineral replacement mechanisms. The resulting pore system maintains effective porosity of 2%–20% with excellent connectivity through multiple scales of pore networks, from micropores providing storage to larger intercrystalline and dissolution pores providing flow pathways. The intermediate-performing mud-supported microfacies (MF3, MF5, MF7) illustrate gradational reservoir quality controlled by varying degrees of mud content and diagenetic modification. MF3 (peloidal bioclast packstone) exhibits moderate permeability due to the presence of peloids that provide some framework support within the mud-supported texture. MF5 (echinoids bioclast packstone) demonstrates poor reservoir quality due to its more mud-supported nature, with effective porosity limited to 0.7%–5% and correspondingly low permeability values. MF7 (planktonic foraminifera packstone) shows low to moderate permeability controlled by micrite content, with effective porosity of 3%–4% representing a compromise between microporosity abundance and limited connectivity. The relationship between microporosity and permeability across all microfacies reveals critical insights into pore structure controls. High microporosity levels characterize most mud-supported microfacies (MF3–MF9), but permeability effectiveness depends entirely on the development of larger pore throats and connectivity networks through diagenetic processes. The dolomitization process emerges as the most significant permeability enhancer, creating intercrystalline spaces that serve as critical flow conduits between storage micropores. Pyritization provides additional enhancement through mineral replacement and potential dissolution of pyrite crystals under specific geochemical conditions. The depositional environment influence becomes apparent when examining the outer ramp microfacies, where fine-grained sediment deposition creates optimal conditions for subsequent diagenetic enhancement. The abundant reactive surface area in fine-grained sediments facilitates extensive dolomitization and pyritization, while the initially low permeability focuses diagenetic fluids along preferred pathways, enhancing the development of connected secondary porosity systems. This explains why outer ramp microfacies like MF9 achieve superior reservoir quality despite unfavorable primary depositional characteristics. The comprehensive analysis demonstrates that pore structure impact on permeability in carbonate microfacies is fundamentally controlled by the complex interplay between primary depositional texture and secondary diagenetic modification, with diagenetic processes often serving as the ultimate determinant of reservoir quality. The counterintuitive superior performance of mud-supported microfacies over grain-supported ones in several cases underscores the critical importance of understanding both depositional and post-depositional controls for accurate carbonate reservoir characterization and development planning.

4.3. Computational considerations

Variational inference stands as a potent method for addressing intricate inverse problems spanning diverse scientific domains. Nevertheless, the approach necessitates an extensive number of Monte Carlo samples from the proposed variational family in each iteration, involving 5000 samples. Over 200 iterations on the sampled set are required to achieve convergence. Our computations, conducted on a high-performing computer with an 11th Gen Intel(R) Core (TM) i7-11370H @ 3.30 GHz processor, reveal that a single iteration consumes nearly 600 s. Consequently, determining variational family parameters for a single data point demands an impractical 40-h computational effort. Given 923 data points in our well log dataset, the overall computational demand extends to an unmanageable four-year timeframe for completion. To address this formidable challenge, we propose a pragmatic solution: providing access to a high-performance computing system equipped with a substantial number of threads, located at University of Houston, and write the codes to distribute the tasks on the available threads using parallel computing techniques. This resource significantly reduces the time required to solve the variational Bayes problem for our extensive dataset. Distributing Monte Carlo sampling and simultaneously processing sampled data points across multiple threads holds the potential to transform our research approach. Preliminary simulations demonstrate that utilizing a high-performance supercomputer with a substantial thread count results in a significant reduction in computation time. This not only renders the research feasible within a reasonable timeframe but also unlocks opportunities for exploring more intricate and computationally demanding inverse problems, pushing the boundaries of scientific inquiry. In resolving the aforementioned challenge, we leveraged the supercomputer infrastructure available at Huston University, which provides 40 clusters, each with 25 threads, totaling 1000 threads. This opportunity allowed us to perform all computations in approximately 6 days.

4.4. Advantages and drawbacks of variational inference over Markov chain Monte Carlo (MCMC)

MCMC methods and fixed form variational inference (FFVB, we also use FFVB interchangeably, “B” stands for Bayes) offer distinct approaches to Bayesian inference. MCMC relies on Markov chains to sample from posterior distributions, guaranteeing convergence but potentially suffering from slow computation, while FFVB optimizes predefined variational families for faster computation, especially in high-dimensional or large datasets. MCMC exhibits robustness in sampling complex posterior distributions but may require extensive tuning, whereas FFVB's deterministic nature and reliance on predefined families may limit its applicability in certain scenarios. For our case we deal with a high dimensional sampling problem which should be done for over 923 data points separately. While we utilized a large number of randomly sampled values from the suggested distributions to diminish variance Eqs. (25) and (26) address Eq. (20), the procedure can be readily parallelized across proficient computational resources.

The best way to perform parallelized sampling using any of the mentioned MCMC algorithms is to implement the operations in a vectorized manner. For this, the function used in inversion should accept a vector input and produce a vector output. In our case, if we could input the model parameters as an $M \times N$ matrix, where, M is the number of depths and N is the number of model parameters, and parallelize this operation on a GPU, we would achieve results much faster. However, the problem lies in the RPT models, which include operations such as two-dimensional numerical integration (used in computing the depolarization and concentration tensors, as described in Eqs. (2) and (11)) and tensor algebra (contraction, inversion), which impede vectorization. Using complex rock physics models such as the general singular approximation (Shermergor, 1977), high-frequency T-matrix approach (Jakobsen et al., 2003a,b), and attenuative T-matrix (Jakobsen et al., 2003a,b; Jakobsen and Chapman, 2009) presents a significant challenge.

5. Conclusion

Our principal objective was to estimate permeability through effective rock physics modeling by solving the inversion problem using sonic and resistivity logs. To validate our findings, we incorporated detailed geological information, including microfacies and sedimentary environment analyses. The application of variational Bayes in conjunction with the trust region optimization algorithm enabled us to derive probability density functions for textural parameters, sonic wave velocity, resistivity, and permeability, thereby incorporating uncertainty in subsurface characteristic estimates. Given that the trust region algorithm necessitates the Hessian for the target function, we extended the simple stochastic gradient descent algorithm with momentum to obtain an analytical solution for the Hessian of the lower bound (LB) function for variational Bayes. The control variate algorithm was then implemented to reduce the variance of datasets generated from the obtained probability density functions. To expedite computations, parallel computing code techniques were employed to distribute computational tasks across available threads. The supercomputer facility at Huston University, equipped with 1000 computing threads, was instrumental in solving the inverse problem using variational Bayes. We also, utilized the Metropolis-Hastings algorithm to obtain samples from the actual posterior distributions at three different depths and compare the results with results obtained by FFVB inversion. The rationale for choosing a limited number of depths for Metropolis-Hastings sampling was due to the constraints of implementing the proposed RPT in a vectorized format and the inherently time-intensive process of the hierarchical Metropolis-Hastings sampling method. Furthermore, we applied the Kullback-Leibler divergence as a measure to assess the similarity between the posterior distributions derived from the Metropolis-Hastings sampling and the family of variational distributions acquired via the FFVB technique.

Our computations lead us to the following conclusions: Variational Bayes, coupled with the trust region optimization algorithm, prove to be a powerful technique devoid of divergence problems associated with stochastic gradient descent. The main drawback of this algorithm lies in its computational demands due to the necessity of high sampling numbers (in our case, 5000 samples), requiring high-performance computational resources. Estimated sonic travel time and true formation resistivity align well with the actual measured log data, demonstrating the success in solving the inverse problem and the efficacy of the proposed rock physics template for the studied carbonate formation (the Ilam Formation). Estimated permeability values show a strong correlation with measured permeability data on core samples at average reservoir pressure. These values exhibit robust consistency with actual geological and microfacies analyses, particularly where experimental data are absent. The low values of Kullback–Leibler distances computed for the three depths also demonstrate the accuracy of the proposed variational family and inversion algorithm employed to minimize the variational function. The primary challenge persists in the computational efficiency of the rock physics models utilized. We acknowledge that sophisticated multi-threaded and multi-cluster computational facilities are not universally accessible. Moving forward, our focus will be on effectively addressing this issue by developing algorithms that can operate efficiently on simpler computational resources, such as personal laptops. This approach aims to broaden accessibility and facilitate broader application of our methodologies in future studies.

CRediT authorship contribution statement

Mohammadfarid Ghasemi: Writing – review & editing, Writing – original draft, Visualization, Validation, Supervision, Software, Resources, Project administration, Methodology, Investigation, Formal analysis, Data curation, Conceptualization. **Abdorrazagh Javid:** Conceptualization.

Funding statement

This research did not receive any specific grant from funding agencies in the public, commercial, or not-for-profit sectors.

Conflict of interest statement

The authors declare that they have no known competing financial interests or personal relationships that could have appeared to influence the work reported in this manuscript.

Appendix A. Supplementary data

Supplementary data to this article can be found online at https://doi.org/10.1016/j.petsci.2025.10.011.

Appendix A

Surface and bulk conductivity of voids

The second rank tensor of conductivity coefficient $R^{(\mathrm{r})}$ as follows:

$$R^{(\mathrm{r})}=\sum\nolimits_{\mathrm{c}}\cdot I_2, \tag{A.1}$$

where, $\sum_{\mathrm{c}}$ is the total rock conductivity, I_2 is the identity for second rank tensors.

$$\sum\nolimits_{\mathrm{c}}=\sum_i \sigma_{\mathrm{c},i,} \tag{A.2}$$

where $\sigma_{c,i}$ is the i th ionic contribution to rock conductivity and the sum is over all the ionic species present in the pore fluid.

$$\sigma_{\mathrm{c},i}=t_i^{\mathrm{f,hf}}\sigma_{\mathrm{f}}\hat{\mathrm{G}}\left[\frac{t_i^{\mathrm{S,hf}}\sum_{\mathrm{S}}}{t_i^{\mathrm{f,hf}}\sigma_{\mathrm{f}}}\right], \tag{A.3}$$

where,

$$\hat{\mathrm{G}}[X]=\frac{b+cX+dX^2}{1+aX}, \tag{A.4}$$

$$a=\frac{\frac{2}{(\Lambda F)}-\frac{1}{f}}{\frac{\lambda}{2f}-\frac{1}{F}}, \tag{A.5}$$

$$c=\frac{1-\lambda/\Lambda}{f-\lambda F/2}, \tag{A.6}$$

$$b=\frac{1}{F}, d=\frac{a}{f}, \tag{A.7}$$

$$F=1, f=\tau\left(\frac{2\mathrm{Vp}}{\mathrm{Sp}}\right), \tag{A.8}$$

$$\frac{2}{\lambda}=\frac{2}{\Lambda}=\frac{\mathrm{Sp}}{\mathrm{Vp}}, \tag{A.9}$$

where Sp, Vp is the area and the volume of an arbitrary ellipse, respectively, and τ is tortuosity. The parameters λ and Λ are the characteristic dimensions associated with pore and surface transport, respectively. In the pore space scale these two microstructural parameters are same (Revil and Glover, 1997). The free electrolyte conductivity is:

$$\sigma_{\mathrm{f}}=\sum_i eZ_i\beta_i^{\mathrm{f}}C_i^{\mathrm{f}}, \tag{A.10}$$

where C_i^{f} is the concentration of ionic species i in the free electrolyte. Effective mobilities B_i defined by $B_i\equiv\beta_i+2\varepsilon_{\mathrm{f}}k_{\mathrm{B}}T/\eta_{\mathrm{f}}eZ_i$ where η_{f} is the fluid dynamic viscosity ($\eta_{\mathrm{f}}\approx 10^{-3}$ Pa for water at 25 °C), T is the temperature, ε_{f} is the fluid dielectric permittivity (in F m^{-1}), k_{B} is the Boltzmann's constant (1.381×10^{-23} J K^{-1}), e is the electron charge (1.602×10^{-19} Coulombs), and Z_i the valence of ion (all quantities including e and the ionic valences are taken to be positive). β_i is the classic ionic mobility and can be found for each ion type in Physical Chemistry Handbooks such as (Brummer et al., 1971).

Transference and Hittorf numbers of species i (respectively, t_i^{f} and $t_i^{\mathrm{f,hf}}$) in the free electrolyte are defined by:

$$t_i^{\mathrm{f}}\equiv\frac{(\pm1)\beta_i^{\mathrm{f}}eC_i^{\mathrm{f}}}{\sigma_f}, \tag{A.11}$$

$$t_i^{\mathrm{f,hf}}\equiv(\pm1)Z_i t_i^{\mathrm{f}}, \text{and} \quad \sum_i\left(t_i^{\mathrm{f,hf}}\right)=1, \tag{A.12}$$

The parameters $t_i^{\mathrm{f,hf}}$ represent the ratio between the electrical current due to species i divided by the total electrical current in the free electrolyte. According to their definition, the Hittorf numbers are positive for all ions (with $0\leq t_i^{\mathrm{f,hf}}\leq 1$).

The specific surface conductance, $\sum_{\mathrm{S}}$, represents the anomalous conduction in the EDL. In the present approach, we do not consider electrical conduction in the Stern layer or directly through the surface sites, and consequently surface conduction only takes place in the EDL. The specific surface conductance can be described from the sum of the individual specific surface conductance in the EDL by:

$$\sum\nolimits_{\mathrm{S}}=\sum_i eZ_i\sum\nolimits_i^{\mathrm{S}}. \tag{A.13}$$

The ionic contributions $\sum_i^{\mathrm{S}}$ are dimensionally different from $\sum_{\mathrm{S}}$. Surface transference and Hittorf numbers of species i

(respectively, t_i^{S} and $t_i^{\mathrm{S,hf}}$) can be now defined by analogy with t_i^{f} and $t_i^{\mathrm{f,hf}}$:

$$t_i^S \equiv (\pm 1)e\sum\nolimits_i^{\mathrm{S}} \Big/ \sum\nolimits_{\mathrm{S}}, \tag{A.14}$$

$$t_i^{\mathrm{S,hf}} \equiv (\pm 1)Z_i t_i^{\mathrm{f}}, \text{and} \quad \sum_i \left(t_i^{\mathrm{S,hf}}\right) = 1, \tag{A.15}$$

where $t_i^{\mathrm{S,hf}}$ represents the difference of electrical charges fraction transported by species i during electrical conduction (including an electro-osmotic contribution) between the EDL and the free electrolyte (the matrix is always chosen as the reference frame). We have $0 \le t_i^{\mathrm{S,hf}} \le 1$.

The total specific surface conductance $\sum_{\mathrm{S}}$, can be divided into an electromigration conductance $\sum_{\mathrm{S}}^{\mathrm{e}}$ and an electro-osmotic conductance $\sum_{\mathrm{S}}^{\mathrm{os}}$.

$$\sum\nolimits_{\mathrm{S}} = \sum\nolimits_{\mathrm{S}}^{\mathrm{e}} + \sum\nolimits_{\mathrm{S}}^{\mathrm{os}}. \tag{A.16}$$

The two surface conductance terms introduced previously can be described using the sum of their ionic contributions $\sum_{\mathrm{S}}^{\mathrm{e}} \equiv e\sum_i \left(Z_i \sum_i^{\mathrm{e}}\right)$, $\sum_{\mathrm{S}}^{\mathrm{os}} = e\sum_i \left(Z_i \sum_i^{\mathrm{os}}\right)$ consequently:

$$\sum\nolimits_i^{\mathrm{S}} = \sum\nolimits_i^{\mathrm{e}} + \sum\nolimits_i^{\mathrm{os}}. \tag{A.17}$$

The Stern plane potential is calculated with following equation:

$$\phi = -\frac{e\varphi}{k_B T}, \tag{A.18}$$

where φ is the dimensionless reduced local potential in the EDL, k_{B} is the Boltzmann's constant (1.381×10^{-23} J K^{-1}), e is the electron charge, and T is the temperature.

The Stern plane potential must satisfy the following equation:

$$F[X] = 0, \tag{A.19}$$

where the function $F[X]$ is given by:

$$\begin{aligned} F[X] = {} & \frac{\eta}{2}\sqrt{C_{\mathrm{f}} + 10^{-pH} + 10^{pH - pK_{\mathrm{w}}}}\left(X - \frac{1}{X}\right) * \\ & \left(1 + K_{(+)}10^{-pH}X^2 + \frac{K_{\mathrm{Na}}}{10^{-pH}}C_{\mathrm{Na^+}}^{\mathrm{f}} + K_{\mathrm{Cl}}C_{\mathrm{Cl^-}}^{\mathrm{f}}\,10^{-pH}\right) \\ & + K_{(+)}10^{-pH}X^2 - \frac{K_{(-)}}{10^{-pH}}X^{-2}, \end{aligned} \tag{A.20}$$

where, $\eta = \sqrt{8\varepsilon_{\mathrm{f}} k_{\mathrm{B}} T N 10^3} \Big/ \left(eT_{\mathrm{S}}^0\right)$, and $X \equiv \exp\,(\phi/2)$, T_{S}^0 is total surface site density, C_{f} is the electrolyte concentration, for the direct problem pH and C_{f} are the input parameters, and φ is the output parameter. ε_{f} is the fluid dielectric permittivity (dielectric constant of water $\varepsilon_{\mathrm{f}} \approx \varepsilon_0 80$, and $\varepsilon_0 = 8.84 \times 10^{-12}$ F m), $N = 6.022 \times 10^{23}$ is Avogadro's constant, $pK_{\mathrm{w}} = -\log_{10} K_{\mathrm{w}}$, K_{w} is the disassociation constant of water (K_{w} close to $10^{-13.8}$ at 20 °C), $C_{\mathrm{Cl^-}}^{\mathrm{f}} = C_{\mathrm{f}} + C_{\mathrm{a}}$, $C_{\mathrm{a}} = 10^3 N 10^{-pH}$ is acid concentration (mol/L), $C_{\mathrm{Na^+}}^{\mathrm{f}} = C_{\mathrm{f}} + C_{\mathrm{b}}$, and $C_{\mathrm{b}} = 10^3 N 10^{pH - pK_{\mathrm{w}}}$ is base concentration (mol/L). $K_{(+)}, K_{(-)}$ are the intrinsic equilibrium constants.

References

Ahmadi, M.A., Zendehboudi, S., Lohi, A., 2013. Reservoir permeability prediction by neural networks combined with hybrid genetic algorithm and particle swarm optimization. Geophys. Prospect. 61, 582–598. https://doi.org/10.1111/j.1365-2478.2012.01080.x.

Ahmed, U., Crary, S.F., Grace, G.R., 1991. Permeability estimation: The various sources and their interrelationships. J. Petrol. Technol. 43, 578–587. https://doi.org/10.2118/19604-PA.

Al-Anazi, A., Gates, I.D., 2010. Support-vector regression for permeability prediction in a heterogeneous reservoir: A comparative study. SPE Reservoir Eval. Eng. 13, 485–495. https://doi.org/10.2118/126339-PA.

Al Mahrouqi, D., Vinogradov, J., Jackson, M.D., 2017. Zeta potential of artificial and natural calcite in aqueous solution. Adv. Colloid Interface Sci. 240, 60–76. https://doi.org/10.1016/j.cis.2016.12.006.

Al Moqbel, A., Wang, Y., 2011. Carbonate reservoir characterization with lithofacies clustering and porosity prediction. J. Geophys. Eng. 8, 592–598. https://doi.org/10.1088/1742-2132/8/4/021.

Al-Mudhafar, W.J., Mohamed, L., 2015. Incorporating lithofacies classification and well logs into statistical learning algorithms for comparative multisource permeability modelling. In: SPE North Africa Technical Conference and Exhibition. https://doi.org/10.2118/175805-MS.

Al-Raoush, R., Willson, C.S., 2005. Extraction of physically realistic pore network properties from three-dimensional synchrotron X-ray microtomography images of unconsolidated porous media systems. J. Hydrol. 300, 44–64. https://doi.org/10.1016/j.jhydrol.2004.05.005.

Ali, A., 2011. Correlations Between the Effective Permeability and Seismic Anisotropy of Fractured Reservoirs. University of Bergen, Bergen, Norway. PhD Thesis.

Ali, A., Jakobsen, M., 2014. Anisotropic permeability in fractured reservoirs from frequency-dependent seismic amplitude versus angle and azimuth data. Geophys. Prospect. 62, 293–314. https://doi.org/10.1111/1365-2478.12082.

Archie, G.E., 1942. The electrical resistivity log as an aid in determining some reservoir characteristics. Transac. AIME 146, 54–62. https://doi.org/10.2118/942054-G.

Barthélémy, J.F., 2009. Effective permeability of media with a dense network of long and micro fractures. Transport Porous Media 76, 153–178. https://doi.org/10.1007/s11242-008-9241-9.

Bateman, R., 1985. Open-Hole Log Analysis and Formation Evaluation. International Human Resources Development Corporation, Boston, Massachusetts.

Batzle, M., Wang, Z., 1992. Seismic properties of pore fluids. Geophysics 57, 1396–1408. https://doi.org/10.1190/1.1443207.

Bayuk, I.O., 2013. Fundamentals of mathematical modeling of macroscopic physical properties of hydrocarbon reservoirs. Seismic Technol. 4, 5–18 (in Russian).

Bayuk, I.O., Chesnokov, E.M., 1998. Correlation between elastic and transport properties of porous cracked anisotropic media. Phys. Chem. Earth 23, 361–366. https://doi.org/10.1016/S0079-1946(98)00035-4.

Bayuk, I.O., Ammerman, M., Chesnokov, E.M., 2007. Elastic moduli of anisotropic clay. Geophysics 72, D107–D117. https://doi.org/10.1190/1.2757624.

Bayuk, I.O., Ammerman, M., Chesnokov, E.M., 2008. Upscaling of elastic properties of anisotropic sedimentary rocks. Geophys. J. Int. 172, 842–860. https://doi.org/10.1111/j.1365-246X.2007.03645.x.

Beaumont, M.A., 2003. Estimation of population growth or decline in genetically monitored populations. Genetics 164, 1139–1160. https://doi.org/10.1093/genetics/164.3.1139.

Berger, J.O., Bernardo, J.M., 1991. On the development of reference priors. Bayesian Stat. 4, 35–60.

Bethe, H., 1931. Zur Theorie der Metalle. Z. Phys. 71, 205–226. https://doi.org/10.1007/BF01341708 (in German).

Blei, D.M., Kucukelbir, A., McAuliffe, J.D., 2017. Variational inference: A review for statisticians. J. Am. Stat. Assoc. 112, 859–877. https://doi.org/10.1080/01621459.2017.1285773.

Bosch, M., Mukerji, T., Gonzalez, E.F., 2010. Seismic inversion for reservoir properties combining statistical rock physics and geostatistics: a review. Geophysics 75, 75A165–75A176. https://doi.org/10.1190/1.3478209.

Bourdet, D., Ayoub, J.A., Pirard, Y.M., 1989. Use of pressure derivative in well-test interpretation. SPE Form. Eval. 4, 293–302. https://doi.org/10.2118/12777-PA.

Bouwer, H., Rice, R.C., 1976. A slug test for determining hydraulic conductivity of unconfined aquifers with completely or partially penetrating wells. Water Resour. Res. 12, 423–428. https://doi.org/10.1029/WR012i003p00423.

Bratton, T., Canh, D.V., Van Que, N., Duc, L.V., Gillespie, P., Hunt, D., Li, B., Marcinew, R., Ray, S., Montaron, B., Nelson, R., Schoderbek, D., Sonneland, L., 2006. The nature of naturally fractured reservoirs. Oilfield Rev. 18, 4–23.

Brummer, S.B., Turner, D.R., Makrides, A.C., 1971. Investigation of Ion Mobility in Aqueous Solutions. U.S. Department of the Interior, Office of Saline Water, Washington, D.C.

Byrd, R.H., Schnabel, R.B., Shultz, G.A., 1987. A trust region algorithm for nonlinearly constrained optimization. SIAM J. Numer. Anal. 24, 1152–1170. https://doi.org/10.1137/0724076.

Carcione, J.M., Avseth, P., 2015. Rock-physics templates for clay-rich source rocks. Geophysics 80, D481–D500. https://doi.org/10.1190/geo2014-0510.1.

Chen, C., Liebermann, R.C., Weidner, D.J., 2001. Elasticity of single-crystal calcite and rhodochrosite by Brillouin spectroscopy. Am. Mineral. 86, 1525–1529. https://doi.org/10.2138/am-2001-11-1222.

Chork, C.Y., Jian, F.X., Taggart, I.J., McKibbin, M.J., Edmundson, H., 1994. Porosity and permeability estimation based on segmented well log data. J. Petrol. Sci. Eng. 11, 227–239. https://doi.org/10.1016/0920-4105(94)90046-9.

Crain, E.R., 2021. Petrophysical Handbook. Available online: https://www.spec2000.net/.

DeGraff, J.M., Aydin, A., Dyer, R., 2005. Fracture Network Modeling and dual-permeability Simulation of Carbonate Reservoirs. International Petroleum Technology Conference. https://doi.org/10.2523/IPTC-10924-MS.

Dorfman, M., Forgotson, J.M., Dufour, J., 1990. New Techniques in Lithofacies Determination and Permeability Prediction in Carbonates Using Well Logs. Geological Society, London, Special Publications vol 48, 113–120. https://doi.org/10.1144/GSL.SP.1990.048.01.10.

Duane, S., Kennedy, A.D., Pendleton, B.J., Roweth, D., 1987. Hybrid Monte Carlo. Phys. Lett. B 195, 216–222. https://doi.org/10.1016/0370-2693(87)91197-X.

Ezzedine, S., Rubin, Y., Chen, J., 1999. Bayesian method for hydrogeological site characterization using borehole and geophysical survey data: theory and application to the Lawrence Livermore National Laboratory Superfund site. Water Resour. Res. 35, 2671–2683. https://doi.org/10.1029/1999WR900155.

Flügel, E., 2004. Microfacies of Carbonate Rocks: Analysis, Interpretation and Application. Springer-Verlag, Berlin Heidelberg.

Fokker, P.A., 2001. General anisotropic effective medium theory for the effective permeability of heterogeneous reservoirs. Transport Porous Media 44, 205–218. https://doi.org/10.1023/A:1010755003160.

Geman, S., Geman, D., 1984. Stochastic relaxation, Gibbs distributions, and the Bayesian restoration of images. IEEE Trans. Pattern Anal. Mach. Intell. PAMI-6, 721–741. https://doi.org/10.1109/TPAMI.1984.4767596.

Ghasemi, M.F., Bayuk, I.O., 2020. Bounds for pore space parameters of petroelastic models of carbonate rocks. Izvestiya Phys. Solid Earth 56, 207–224. https://doi.org/10.1134/S1069351320020037.

Ghon, G., Haque, A.E., Janjuhah, H.T., 2018. Carbonate reservoir characterisation of an isolated platform integrating sequence stratigraphy and rock physics in Central Luconia. In: 80th EAGE Conference and Exhibition 2018. https://doi.org/10.3997/2214-4609.201801316.

Goloshubin, G., Van Schuyver, C., Korneev, V., Silin, D., Vingalov, V., 2008. Reservoir permeability from seismic attribute analysis. Lead. Edge 27, 376–381. https://doi.org/10.1190/1.2896628.

Gomez, C.T., Dvorkin, J., Vanorio, T., 2010. Laboratory measurements of porosity, permeability, resistivity, and velocity on Fontainebleau sandstones. Geophysics 75, E191–E204. https://doi.org/10.1190/1.3493633.

Gordon, N.J., Salmond, D.J., Smith, A.F.M., 1993. Novel approach to nonlinear/non-Gaussian Bayesian state estimation. In: IEE Proceedings F (Radar and Signal Processing) 140, pp. 107–113. https://doi.org/10.1049/ip-f-2.1993.0015.

Granberry, R.J., Keelan, D.K., 1977. Critical water estimates for Gulf Coast sands. SPE Form. Eval. 12, 142–148. https://doi.org/10.2118/6009-PA.

Green, P.J., 1995. Reversible jump Markov chain Monte Carlo computation and Bayesian model determination. Biometrika 82, 711–732. https://doi.org/10.1093/biomet/82.4.711.

Hastings, W.K., 1970. Monte Carlo sampling methods using Markov chains and their applications. Biometrika 57, 97–109. https://doi.org/10.1093/biomet/57.1.97.

Heberling, F., Trainor, T.P., Lützenkirchen, J., Eng, P., Denecke, M.A., Bosbach, D., 2011. Structure and reactivity of the calcite–water interface. J. Colloid Interface Sci. 354, 843–857. https://doi.org/10.1016/j.jcis.2010.10.047.

Hoffman, M.D., Gelman, A., 2014. The No-U-Turn sampler: adaptively setting path lengths in Hamiltonian Monte Carlo. J. Mach. Learn. Res. 15, 1593–1623. https://www.jmlr.org/papers/volume15/hoffman14a/hoffman14a.pdf.

Huang, Z., Williamson, M.A., 1996. Artificial neural network modelling as an aid to source rock characterization. Mar. Petrol. Geol. 13, 277–290. https://doi.org/10.1016/0264-8172(95)00062-3.

Hudson, J.A., 1980. Overall properties of a cracked solid. Math. Proc. Camb. Phil. Soc. 88, 371–384. https://doi.org/10.1017/S0305004100057674.

Jakobsen, M., 2006. The Effective Permeability of Fractured Reservoirs and Composite Porous Media. SEG Technical Program Expanded Abstracts, pp. 1747–1751. https://doi.org/10.1190/1.2369861.

Jakobsen, M., 2007. Effective hydraulic properties of fractured reservoirs and composite porous media. J. Seismic Explor. 16, 199–224.

Jakobsen, M., Chapman, M., 2009. Unified theory of global flow and squirt flow in cracked porous media. Geophysics 74, WA65–WA76. https://doi.org/10.1190/1.3078208.

Jakobsen, M., Hudson, J.A., Johansen, T.A., 2003a. T-matrix approach to shale acoustics. Geophys. J. Int. 154, 533–558. https://doi.org/10.1046/j.1365-246X.2003.01977.x.

Jakobsen, M., Hudson, J.A., Minshull, T.A., Singh, S.C., 2003b. The acoustic signature of fluid flow in complex porous media. J. Appl. Geophys. 54, 219–246. https://doi.org/10.1016/j.jappgeo.2003.08.004.

Jiang, T., 2013. Connection of Elastic and Transport Properties: Effective Medium Study in Anisotropic Porous Media. University of Bergen, Bergen, Norway. PhD Thesis.

Jiang, T., Chesnokov, E.M., 2012. Elastic moduli's relation to microstructure properties in porous media using GSA modeling. In: SEG International Exposition and Annual Meeting, pp. 1–5. https://doi.org/10.1190/segam2012-0436.1.

Johnson, W.W., 1994. Permeability determination from well logs and core data. SPE Permian Basin Oil and Gas Recovery Conference. https://doi.org/10.2118/27647-MS.

Kabir, A., Haque, A.E., Hossain, M.M., Ahmed, M., 2011. Reservoir characterisation of Surat Basin coal seams using drill stem tests. In: SPE Asia Pacific Oil and Gas Conference and Exhibition. https://doi.org/10.2118/147173-MS.

Khromova, I., Ezzedine, S., Chapman, M., 2011. Comparison of seismic-based methods for fracture permeability prediction. First Break 29, 87–93. https://doi.org/10.3997/1365-2397.29.1.54880.

Klimentos, T., 1991. The effects of porosity-permeability-clay content on the velocity of compressional waves. Geophysics 56, 1930–1939. https://doi.org/10.1190/1.1443001.

Kohn, W., Sham, L.J., 1965. Self-consistent equations including exchange and correlation effects. Phys. Rev. 140, A1133–A1138. https://doi.org/10.1103/PhysRev.140.A1133.

Kullback, S., Leibler, R.A., 1951. On information and sufficiency. Ann. Math. Stat. 22, 79–86. https://doi.org/10.1214/aoms/1177729694.

Kuster, G.T., Toksöz, M.N., 1974. Velocity and attenuation of seismic waves in two-phase media: part I. theoretical formulations. Geophysics 39, 587–606. https://doi.org/10.1190/1.1440450.

Lee, S.H., Datta-Gupta, A., Singh, V.P., 2002. Electrofacies characterization and permeability predictions in complex reservoirs. SPE Reservoir Eval. Eng. 5, 237–248. https://doi.org/10.2118/78662-PA.

Lehmann, E.L., George, C., 1998. Minimaxity and Admissibility. In: Theory of Point Estimation. Springer Texts in Statistics. Springer, New York, NY. https://doi.org/10.1007/0-387-22728-8_5.

Li, H., Zhang, J., 2018. Well log and seismic data analysis for complex pore-structure carbonate reservoir using 3D rock physics templates. J. Appl. Geophys. 151, 175–183. https://doi.org/10.1016/j.jappgeo.2018.02.017.

Li, S., Leroy, P., Heberling, F., Devau, N., Jougnot, D., Chiaberge, C., 2016. Influence of surface conductivity on the apparent zeta potential of calcite. J. Colloid Interface Sci. 468, 262–275. https://doi.org/10.1016/j.jcis.2016.01.075.

Lin, J.L., Salisch, H., 1994. Determination from well logs of porosity and permeability in a heterogeneous reservoir. In: SPE Asia Pacific Oil and Gas Conference and Exhibition. https://doi.org/10.2118/28675-MS.

Liu, J.S., Chen, R., 1998. Sequential Monte Carlo methods for dynamic systems. J. Am. Stat. Assoc. 93, 1032–1044. https://doi.org/10.1080/01621459.1998.10473765.

Mavko, G., Mukerji, T., Dvorkin, J., 2020. The Rock Physics Handbook, third ed. Cambridge University Press, Cambridge.

Metropolis, N., Rosenbluth, A.W., Rosenbluth, M.N., Teller, A.H., Teller, E., 1953. Equation of state calculations by fast computing machines. J. Chem. Phys. 21, 1087–1092. https://doi.org/10.1063/1.1699114.

Mohaghegh, S., Arefi, R., Ameri, S., Rose, D., 1995. State-of-the-art in permeability determination from well log data: part 2-verifiable, accurate permeability predictions, the touch-stone of all models. SPE East. Region. Meet. https://doi.org/10.2118/30978-MS.

Mohaghegh, S., Arefi, R., Ameri, S., Hefner, M.H., 1997. Permeability determination from well log data. SPE Form. Eval. 12, 170–174. https://doi.org/10.2118/30978-PA.

Mondal, I., Singh, K.H., 2024. Petrophysical insights into pore structure in complex carbonate reservoirs using NMR data. Petrol. Res. 9, 439–450. https://doi.org/10.1016/j.ptlrs.2024.01.006.

Mori, T., Tanaka, K., 1973. Average stress in matrix and average elastic energy of materials with misfitting inclusions. Acta Metall. 21, 571–574. https://doi.org/10.1016/0001-6160(73)90064-3.

Morris, R.L., Biggs, W.P., 1967. Using log-derived values of water saturation and porosity. In: SPWLA 8th Annual Logging Symposium.

Moulin, P., Roques, H., 2003. Zeta potential measurement of calcium carbonate. J. Colloid Interface Sci. 261, 115–126. https://doi.org/10.1016/S0021-9797(03)00057-2.

Nashawi, I.S., Malallah, A., 2009. Improved electrofacies characterization and permeability predictions in sandstone reservoirs using a data mining and expert system approach. Petrophys. SPWLA J. Form. Evaluat. Reservoir Descrip. 50, 250–263.

Nawaz, M.A., Curtis, A., Gerea, C., 2020. Variational bayesian inversion of seismic attributes jointly for geologic facies and petrophysical rock properties. Geophysics 85, MR213–MR233. https://doi.org/10.1190/geo2019-0163.1.

Neal, R.M., 1996. Introduction. Bayesian Learning for Neural Networks. Springer-Verlag, New York, pp. 1–28.

Nie, R., Meng, Y., Jia, Y., Zhang, F., Yang, X., Niu, X., 2012. Dual porosity and dual permeability modeling of horizontal well in naturally fractured reservoir. Transport Porous Media 92, 213–235. https://doi.org/10.1007/s11242-011-9898-3.

Norris, A.N., 1985. A differential scheme for the effective moduli of composites. Mech. Mater. 4, 1–16. https://doi.org/10.1016/0167-6636(85)90002-X.

Peselnick, L., Robie, R.A., 1962. Elastic constants of calcite. J. Appl. Phys. 33, 2889–2892. https://doi.org/10.1063/1.1728999.

Poupon, A., Leveaux, J., 1971. Evaluation of water saturation in shaly formations. In: SPWLA 12th Annual Logging Symposium. Dallas, Texas, 2-5 May 1971.

Prasad, M., 2003. Velocity-permeability relations within hydraulic units. Geophysics 68, 108–117. https://doi.org/10.1190/1.1543198.

Pride, S.R., Harris, J.M., Johnson, D.L., Mateeva, A., Nihei, K.T., Nowack, R.L., Rector, J.W., Spetzler, H., Wu, R., Yamamoto, T., Berryman, J.G., Fehler, M., 2003. Permeability dependence of seismic amplitudes. Lead. Edge 22, 518–525. https://doi.org/10.1190/1.1587671.

Purvance, D.T., Andricevic, R., 2000. Geoelectric characterization of the hydraulic conductivity field and its spatial structure at variable scales. Water Resour. Res. 36, 2915–2924. https://doi.org/10.1029/2000WR900187.

Rafik, B., Kamel, B., 2017. Prediction of permeability and porosity from well log data using the nonparametric regression with multivariate analysis and neural network, Hassi R'Mel Field, Algeria. Egypt. J. Pet. 26, 763–778. https://doi.org/10.1016/j.ejpe.2016.10.013.

Raymer, L.L., Hunt, E.R., Gardner, J.S., 1980. An improved sonic transit time-to-porosity transform. In: SPWLA 21st Annual Logging Symposium.

Revil, A., 2013. Effective conductivity and permittivity of unsaturated porous materials in the frequency range 1 mHz–1GHz. Water Resour. Res. 49, 306–327. https://doi.org/10.1029/2012WR012700.

Revil, A., Glover, P.W.J., 1997. Theory of ionic-surface electrical conduction in porous media. Phys. Rev. B 55, 1757–1773. https://doi.org/10.1103/PhysRevB.55.1757.

Revil, A., Glover, P.W.J., 1998. Nature of surface electrical conductivity in natural sands, sandstones, and clays. Geophys. Res. Lett. 25, 691–694. https://doi.org/10.1029/98GL00296.

Revil, A., Pezard, P.A., Glover, P.W.J., 1999. Streaming potential in porous media: 2. Theory and application to geothermal systems. J. Geophys. Res. Solid Earth 104, 20033–20048. https://doi.org/10.1029/1999JB900089.

Robert, C.P., 2007. From Prior Information to Prior Distributions. the Bayesian Choice: from decision-theoretic Foundations to Computational Implementation, second ed. Springer, New York, pp. 105–163.

Rogers, S., Fang, J.H., Karr, C.L., Stanley, D.A., 1995. Predicting permeability from porosity using artificial neural networks. AAPG (Am. Assoc. Pet. Geol.) Bull. 79, 1786–1797. https://doi.org/10.1306/7834E0F5-1721-11D7-8645000102C1865D.

Saidian, M., Prasad, M., Bahrami, H., 2021. Pore-structure characterization of a complex carbonate reservoir in South Iraq using advanced interpretation of NMR logs. Petrophys. SPWLA J Form. Evaluat. Reser. Descrip. 62, 138–155. https://doi.org/10.30632/PJV62N2-2021a2.

Sams, M.S., Andrea, M., 2001. The effect of clay distribution on the elastic properties of sandstones. Geophys. Prospect. 49, 128–150. https://doi.org/10.1046/j.1365-2478.2001.00230.x.

Saner, S., Cagatay, N., Cokgor, S., 1997. Estimation of permeability from well logs using resistivity and saturation data. SPE Form. Eval. 12, 27–31. https://doi.org/10.2118/30978-PA.

Sævik, P.N., Berre, I., Jakobsen, M., Lien, M., 2012. Electrical Conductivity of Fractured Media: a Computational Study of the self-consistent Method. SEG Technical Program Expanded Abstracts, pp. 1–5. https://doi.org/10.1190/segam2012-1474.1.

Sævik, P.N., Berre, I., Jakobsen, M., Lien, M., 2013a. Effective conductivity of fractured rocks by analytical methods: a 3D computational study. Transport Porous Media 100, 115–142. https://doi.org/10.1007/s11242-013-0208-0.

Sævik, P.N., Berre, I., Jakobsen, M., Lien, M., 2013b. A 3D computational study of effective medium methods applied to fractured media. Transport Porous Media 100, 115–142. https://doi.org/10.1007/s11242-013-0208-0.

Sævik, P.N., Berre, I., Jakobsen, M., Lien, M., 2014. Anisotropic effective conductivity in fractured rocks by explicit effective medium methods. Geophys. Prospect. 62, 1297–1314. https://doi.org/10.1111/1365-2478.12173.

Sayers, C.M., den Boer, L.D., 2018. The elastic properties of clay in shales. J. Geophys. Res. Solid Earth 123, 5965–5974. https://doi.org/10.1029/2018JB015942.

Semmelbeck, M., Diyashev, I., 1996. Application of PermLog-A new log-based permeability estimation method. In: SPE Unconventional Resources Conference/Gas Technology Symposium. https://doi.org/10.2118/35678-MS.

Semmelbeck, M., Diyashev, I., Turanli, K., 1995. Invasion-based method for estimating permeability from logs. In: SPE Annual Technical Conference and Exhibition. https://doi.org/10.2118/30978-MS.

Shahraini, A., Javadpour, F., Sepehrnoori, K., 2010. Seismic history matching in fractured reservoirs using a consistent stiffness-permeability model–Focus on the aperture. In: 72nd EAGE Conference and Exhibition incorporating SPE EUROPEC 2010. https://doi.org/10.3997/2214-4609.201400856.

Shermergor, T.D., 1977. Theory of Elasticity of Microinhomogeneous Media. Nauka, Moscow (in Russian).

Simandoux, P, 1963. Dielectric Measurements on Porous Media and Application to Shaly Formations. SPWLA Shaly Sand Reprint 4, 97–124.

Spikes, K., Mukerji, T., Dvorkin, J., Mavko, G., 2007. Probabilistic seismic inversion based on rock-physics models. Geophysics 72, R87–R97. https://doi.org/10.1190/1.2760162.

Tang, X., Cheng, C.H., 1996. Fast inversion of formation permeability from Stoneley wave logs using a simplified Biot-Rosenbaum model. Geophysics 61, 639–645. https://doi.org/10.1190/1.1443993.

Timur, A., 1968. An investigation of permeability, porosity, and residual water saturation relationships. In: SPWLA 9th Annual Logging Symposium.

Torquato, S., 2002. Effective-Medium Approximations. Random Heterogeneous Materials: Microstructure and Macroscopic Properties. Springer-Verlag, New York, pp. 459–484.

Tran, M.N., Nguyen, N., Nott, D., Kohn, R., 2021. A practical tutorial on variational Bayes. arXiv preprint arXiv:2103.01327.

Uba, H.M., Abdel Azim, R., Marafi, A., 2007. Application of a hybrid dual porosity/dual-permeability representation of large-scale fractures to the simulation of a giant carbonate reservoir. In: SPE Middle East Oil and Gas Show and Conference. https://doi.org/10.2118/105616-MS.

van Golf-Racht, T.D., 1982. Fundamentals of Fractured Reservoir Engineering. Elsevier, Amsterdam.

Wang, H., Samuel, M., Dutta, D., Peng, S., Al-Harbi, B., 2009. Velocity Prediction Models Evaluation and Permeability Prediction for Fractured and Caved Carbonate Reservoir: from Theory to Case Study. SEG Technical Program Expanded Abstracts, pp. 2194–2198. https://doi.org/10.1190/1.3255364.

Wang, Y., Aguilera, R., Sheng, G., 2015. Estimation of permeability for tight sandstone reservoir using conventional well logs based on mud-filtrate invasion model. Energy Explor. Exploit. 33, 15–24. https://doi.org/10.1260/0144-5987.33.1.15.

Wang, Z., Long, G., Feagin, M., Sheng, J., 2017. Carbonate rock physics modelling at ultrasonic and seismic frequencies. In: 4th International Workshop on Rock Physics, pp. 28–30. August 2017, Trondheim, Norway.

Watt, J.P., Davies, G.F., O'Connell, R.J., 1976. The elastic properties of composite materials. Rev. Geophys. 14, 541–563. https://doi.org/10.1029/RG014i004p00541.

Waxman, H., Smits, L., 1968. Eectrical conductivities in oil-bearing shaly sands. SPE J. 8 (02), 107–122. https://doi.org/10.2118/1863-A.

Willis, J.R., 1977. Bounds and self-consistent estimates for the overall properties of anisotropic composites. J. Mech. Phys. Solid. 25, 185–202. https://doi.org/10.1016/0022-5096(77)90022-9.

Wilson, J.L., 1975. Principles of Carbonate Sedimentation. Carbonate Facies in Geologic History. Springer-Verlag, New York, pp. 1–19.

Wong, P.Z., Koplik, J., Tomanic, J.P., 1984. Conductivity and permeability of rocks. Phys. Rev. B 30, 6606–6614. https://doi.org/10.1103/PhysRevB.30.6606.

Yao, C.Y., Holditch, S.A., 1993. Estimating permeability profiles using core and log data. In: SPE East. Region. Meet. https://doi.org/10.2118/26921-MS.

Zhang, X., Leeuwenburgh, O., Curtis, A., 2021. Chapter two - an introduction to variational inference in geophysical inverse problems. Adv. Geophys. 62, 73–140. https://doi.org/10.1016/bs.agph.2021.06.003.

Zhao, L., Nasser, M., Han, D.H., 2013. Quantitative geophysical pore-type characterization and its geological implication in carbonate reservoirs. Geophys. Prospect. 61, 827–841. https://doi.org/10.1111/1365-2478.12043.